Geochemistry Geophysics Geosystems G3

Article
Volume 14, Number 9
3 September 2013
doi: 10.1002/ggge.20186
ISSN: 1525-2027

Published by AGU and the Geochemical Society

Cemented mounds and hydrothermal sediments on the detachment surface at Kane Megamullion: A new manifestation of hydrothermal venting

Brian E. Tucholke, Susan E. Humphris, and Henry J. B. Dick

Department of Geology and Geophysics, Woods Hole Oceanographic Institution, Woods Hole, Massachusetts, 02543, USA (btucholke@whoi.edu)

[2] Long-lived detachment faults are now known to be important in tectonic evolution of slow-spreading mid-ocean ridges, and there is increasing evidence that fluid flow plays a critical role in development of detachment systems. Here we document a new manifestation of low-temperature hydrothermal venting associated with the detachment fault that formed Kane Megamullion ~3.3–2.1 m.y. ago in the western rift-valley wall of the Mid-Atlantic Ridge. Hydrothermal effects on the detachment surface include (1) cemented mounds of igneous rock and chalk debris containing hydrothermal Mn oxides and Fe oxyhydroxides, and (2) layered deposits of similar Fe-Mn minerals ± interbedded chalks. Mounds are roughly conical, ~1–10 m high, and contain primarily basalts with lesser gabbro, serpentinite, and polymict breccia. The layered Fe-Mn-rich sediments are flat-bedded to contorted and locally are buckled into low-relief linear or polygonal ridges. We propose that the mounds formed where hydrothermal fluids discharged through the detachment hanging wall near the active fault trace. Hydrothermal precipitates cemented hanging-wall debris and welded it to the footwall, and this debris persisted as mounds as the footwall was exhumed and surrounding unconsolidated material sloughed off the sloping detachment surface. Some of the layered Fe-Mn-rich deposits may have precipitated from fluids discharging from the hanging-wall vents, but they also precipitated from low-temperature fluids venting from the exposed footwall through overlying chalks. Observed natural disturbance and abnormally thin hydrogenous Fe-Mn crusts on some contorted, hydrothermal Fe-Mn-rich chalks on ~2.7 Ma crust suggest diffuse venting that is geologically recent. Results of this study imply that there are significant fluid pathways through all parts of detachment systems and that low-temperature venting through fractured detachment footwalls may continue for several million years off-axis.

Components: 13,414 words, 16 figures, 4 tables.

Keywords: Kane Megamullion; hydrothermal venting; Fe-Mn hydrothermal minerals; oceanic detachment fault; oceanic core complex; Mid-Atlantic Ridge.

Index Terms: 3017 Marine Geology and Geophysics: Hydrothermal systems (1034, 3616, 4832, 8135, 8424); 3035 Mid-ocean ridge processes (1032, 3614, 8416); 3045 Seafloor morphology, geology, and geophysics; 3075 Submarine tectonics and volcanism; 1000 Geochemistry; 3600 Mineralogy and Petrology.

Received 25 January 2013; **Revised** 24 May 2013; **Accepted** 25 May 2013; **Published** 3 September 2013.

Tucholke, B. E., S. E. Humphris, and H. J. B. Dick (2013), Cemented mounds and hydrothermal sediments on the detachment surface at Kane Megamullion: A new manifestation of hydrothermal venting, *Geochem. Geophys. Geosyst.*, *14*, 3352–3378, doi: 10.1002/ggge.20186.

1. Introduction

[3] It has been recognized for three decades that normal faults with very large offsets ("detachment faults") can form in the rift-valley walls of slow-spreading ridges [*Dick et al*., 1981; *Karson*, 1990; *Tucholke and Lin*, 1994]. These faults can slip for ~1–2 m.y., forming oceanic core complexes that expose lower-crustal and upper-mantle rocks. In order to approach isostatic compensation, the detachment footwalls roll over to form megamullions that are characterized by domed shapes and by corrugations (mullion structures) that parallel slip direction and have cross-slip amplitudes up to several hundred meters [*Cann et al*., 1997; *Tucholke et al*., 1996, 1998].

[4] Most studies of detachment faults have concentrated on understanding the kinematics of faulting, morphological development, and the interaction of magmatism and tectonic extension that control the character of the footwall rocks. However, there is increasing evidence that both high- and low-temperature fluid flow plays an important if not key role in the evolution of detachment systems. In particular, fluids may be preferentially channeled along the faults, potentially facilitating their slip by elevating pore-fluid pressure [e.g., *Floyd et al*., 2001] and through fluid-rock reactions that produce weak mineral phases (e.g., serpentine and talc [*Boschi et al*., 2006; *Escartín et al*., 2001; *Schroeder and John*, 2004]). In addition, fluid flow can be important in both detachment hanging walls and in underlying footwalls.

[5] Prime examples of high-temperature hydrothermal venting directly associated with detachment faults are observed south of the Fifteen Twenty Fracture Zone at the Logatchev hydrothermal site (14°44′N) and farther south at 13°19′N to 13°48′N on the Mid-Atlantic Ridge (MAR). Hydrothermal massive sulfides and talc muds in these locations occur along the surfaces and perimeters of core complexes at the sides of the axial rift valley [e.g., *Beltenev*, 2007; *MacLeod et al*., 2009; *Petersen et al*., 2009]. Venting is interpreted to have occurred along the associated detachment faults and, at least at Logatchev, along secondary normal faults in the footwall.

[6] The trans-Atlantic geotraverse (TAG) hydrothermal field at 26°08′N on the MAR provides an example of high-temperature venting through a detachment hanging wall. Although TAG venting has been known since 1985 [*Rona et al*., 1986], its relation to deeper structure was unclear until microearthquake studies were conducted by *deMartin et al*. [2007]. They used microseism hypocenters to map out an embryonic, convex-up detachment fault that extends from beneath the vent field upward to form the eastern rift-valley wall. Hot fluids may be focused along the fault zone at depth, but they are released vertically through the hanging wall before they reach the fault trace at the seafloor.

[7] In contrast, hydrothermal venting from detachment footwalls appears commonly to be low temperature. Fluids averaging ~40°C–75°C in the "Lost City" vents at Atlantis megamullion on the MAR emanate from fractures in serpentinized peridotite about 1.5 m.y. off-axis [*Kelley et al*., 2001] where they are building chimneys composed of calcite, aragonite, and brucite. In the TAG area, diffuse low-temperature venting is present on the emerging detachment footwall and is precipitating low-relief Fe- and Mn-rich hydrothermal deposits [*Thompson et al*., 1985].

[8] Detachment faults are widespread in slow-spreading ocean crust [e.g., *Escartín et al*., 2008; *Smith et al*., 2008; *Tucholke et al*., 2008]. Documenting relationships between these faults and high- and low-temperature fluid flow is important to understanding formation of the detachments as well as their possible association with economically important metal deposits. In this paper, we describe new manifestations of low-temperature hydrothermal venting associated with the detachment system that formed Kane Megamullion on the MAR south of Kane Fracture Zone.

[9] We conducted detailed seafloor surveys of Kane Megamullion (Figure 1) on Knorr Cruise 180-2 in 2004, using the autonomous vehicle ABE and the remotely operated vehicle Jason II in conjunction with a dredging program. The data show two notable features on the surface of the detachment footwall that we attribute to low-temperature

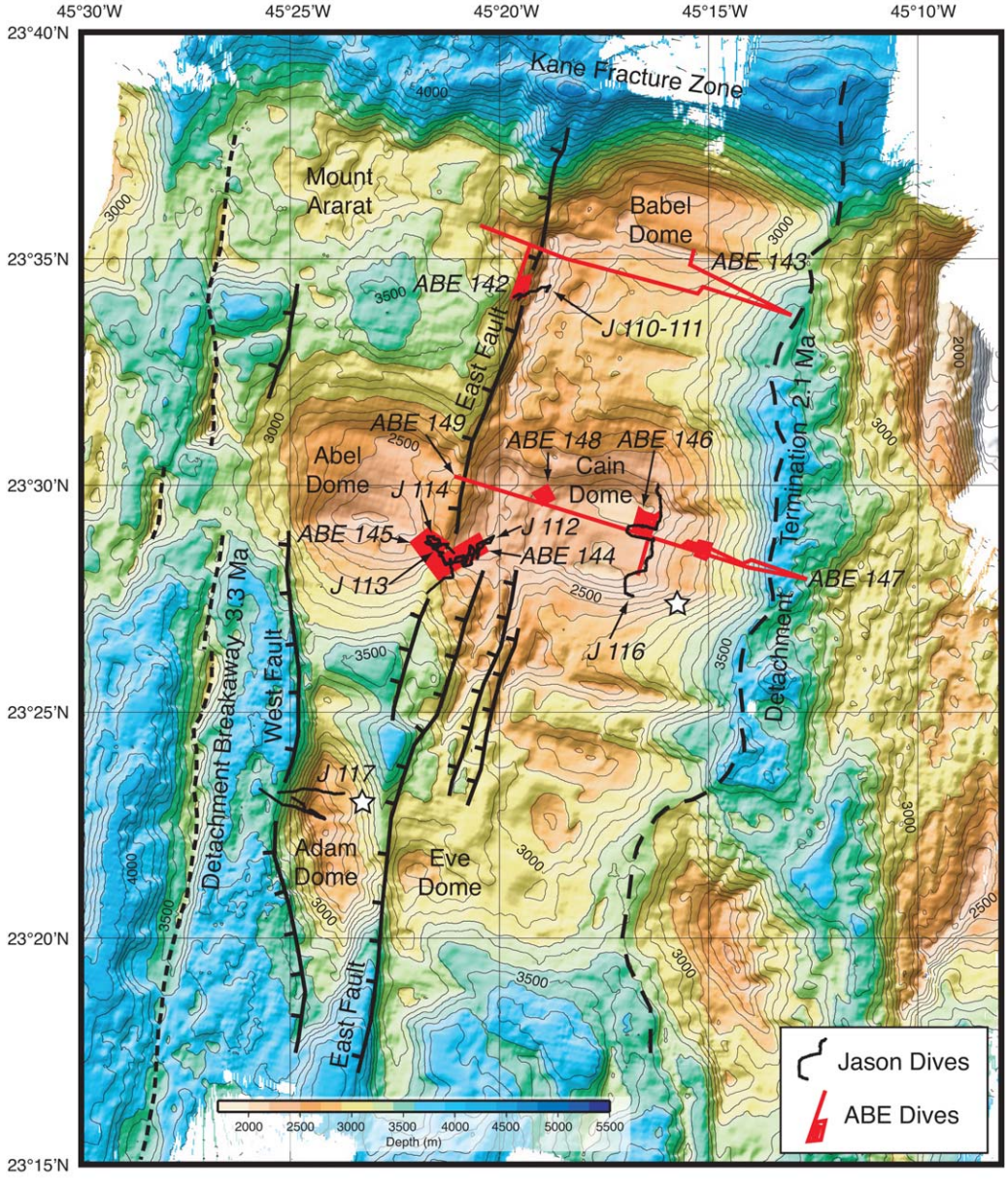

Figure 1. Shaded-relief bathymetric map of Kane Megamullion contoured at 100 m intervals. Locations and simplified structural features are labeled. Areas of ABE surveys are shown in red, and black irregular lines are ROV Jason dive tracks (shown in detail in Figures 2–4). Dredge KN180-2-28, indicated by a star on the east flank of Adam Dome, recovered gastropods of hydrothermal affinity in chalks [*Kaim et al*., 2012]. The star on southeast Cain Dome shows the location of dredge KN180-2-16.

hydrothermal venting: (1) cemented mounds of rock debris that are enriched in hydrothermal Mn oxides and Fe oxyhydroxides, and (2) layered, often highly deformed chalks that cap the detachment surface and are similarly enriched in hydrothermal Fe-Mn precipitates. We propose a model of low-temperature hydrothermal venting through both the hanging wall and footwall to explain these features.

2. Geologic Structure of Kane Megamullion

[10] Kane Megamullion (Figure 1) was formed by a detachment fault that initiated at ~3.3 Ma and was active until ~2.1 Ma in the western rift valley wall of the MAR immediately south of Kane FZ [e.g., *Dick et al*., 2008]. The megamullion is now located ~30–50 km off-axis on the west flank of

the MAR and extends ~40 km south of the fracture zone. The exposed detachment-fault surface is smooth, broadly domed, and incorporates slip-parallel mullion structures that range up to ~600 m in amplitude. There are three groups of domes on the megamullion. In the north, Babel Dome reaches depths less than 2500 m and exhibits two major mullions with amplitudes of ~100 m. It is truncated in the west by East Fault, a west-dipping, high-angle normal fault that cuts through the detachment surface and probably developed in response to bending stresses in the exposed detachment footwall. Mount Ararat to the west has some weakly defined, slip-parallel structure that suggests possible continuity of mullions with Babel Dome, but its otherwise irregular morphology suggests that it is surfaced by volcanics [*Dick et al*., 2008].

[11] Cain and Abel domes in the center of the megamullion are the shallowest domes, with depths reaching less than 2200 m and 2300 m, respectively. There is clear continuity of large mullion structures (amplitudes ca. 100–200 m) between the two domes, but the domes are separated by an offset of ~400 m at East Fault. Farther south, prominent mullions with amplitudes of ~300 m rise to ~2700 m near 25°25′N, but south of this, Adam and Eve domes show little recognizable slip-parallel structure. These two domes are separated by East Fault, with Eve Dome formed by part of the uplifted East Fault footwall. Adam Dome formed as the uplifted footwall of West Fault, another high-angle, west-dipping normal fault that cuts through the detachment surface. West Fault has a throw of up to 1100 m on the steep western side of Adam Dome, while the more gently dipping east flank of the dome is the original detachment surface. Adam Dome reaches depths less than 2500 m.

[12] Extensive sampling of Kane Megamullion has been done by submersible, remotely operated vehicle, and dredging [*Auzende et al*., 1993, 1994; *Dick et al*., 2008]. In situ samples from high-angle fault scarps and slump scars on various parts of the megamullion (Figures 1–4) show that the footwall beneath the damage zone of the detachment fault consists primarily of gabbros and mantle peridotites [*Dick et al*., 2008]. A notable exception occurs at Adam Dome, where West Fault exposes an upward transition from gabbros to sheeted dikes. In situ pillow basalts are associated with East Fault north of Cain Dome, and irregular seafloor morphology around the correlative fault set south of the dome suggests that volcanics may also be present there. Although the morphology of Mount Ararat also suggests the presence of extrusive volcanics, no sampling exists to confirm this.

[13] Unconsolidated calcareous sediments and underlying chalks cover the smooth detachment-fault surface of the megamullion. Chirp-sonar records and video observations (see section 3) indicate that average thickness of these carbonates is a few meters or less. Abundant coarse allochthonous igneous rock debris (centimeter to meter scale) is scattered across, and buried in, the sediment cover. The debris is often in irregular patches, but it also forms distinct mounds and quasi-linear ridges. It is mostly greenschist-facies diabase and pillow basalt that probably was clipped from the detachment hanging wall, but lesser amounts of gabbro and serpentinized peridotite are present. Taking all samples into account, including autochthonous samples from intact basement, sample distribution by weight is about 44% peridotite and dunite, 26% basalt, 24% gabbro, and 5% diabase, with the remaining ~1% divided between polymict breccia and hydrothermal samples [*Dick et al*., 2008].

3. Data Acquisition and Processing

[14] During Knorr Cruise 180-2, we acquired surface-ship multibeam bathymetry (Figure 1) and magnetics [*Williams*, 2007]. The autonomous vehicle ABE was deployed at several locations to acquire high-resolution, near-bottom multibeam bathymetry, sub-bottom chirp-sonar profiles, still photography (ABE Dive 143 on Babel Dome only), and magnetics profiles at varying altitudes above the seafloor (Figure 1). ROV Jason II was used in three of the ABE survey areas to obtain samples and video/still photography (Figures 2–4). There was no ABE survey in the area of Jason Dive 117 on the west flank and crest of Adam Dome (Figure 1).

[15] A total of 386 samples was obtained on seven Jason dives with geological context of all samples documented by recorded video. In addition, 28 dredges were taken at locations broadly distributed across the megamullion [*Dick et al*., 2008], recovering an additional 1142 samples. All samples were cataloged and described according to visual composition and deformation on the ship.

[16] A suite of samples (10 Jason, 2 dredge) with features suggesting hydrothermal influence was

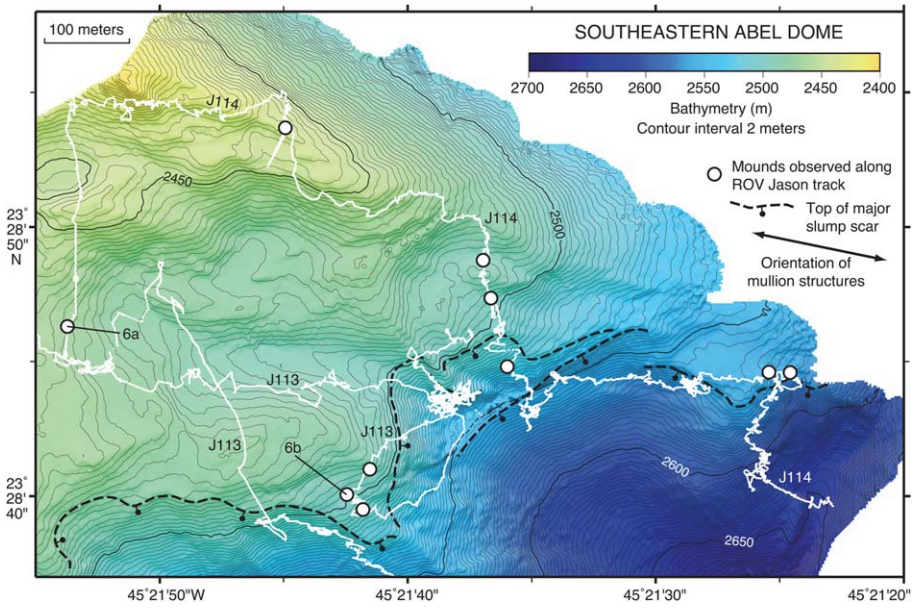

Figure 2. Shaded-relief map showing ABE Dive 145 multibeam bathymetry of the southeast part of Abel Dome (location in Figure 1). Jason 113 and 114 dive tracks (white) are superimposed. Open circles locate mounds observed along dive tracks. Locations of mounds illustrated in subsequent figures are indicated by leaders with figure numbers. The basement is strongly affected by mass wasting, particularly as shown by the major slump scars in the southern part of the map. Jason samples from outcrops exposed in the slump scars indicate that basement is serpentinized harzburgite.

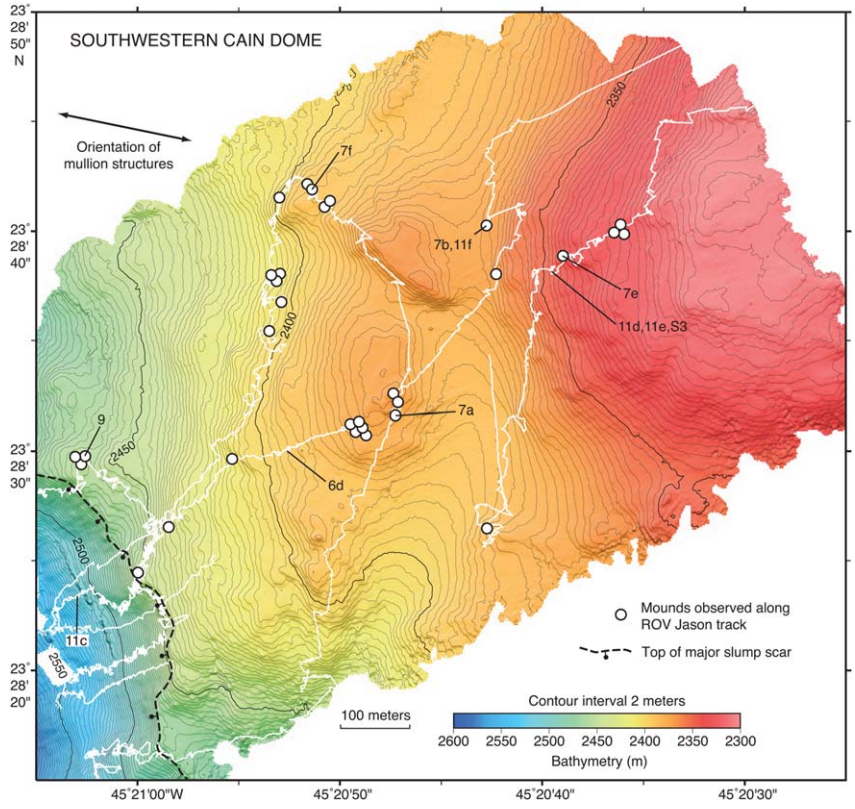

Figure 3. Shaded-relief map showing ABE Dive 144 multibeam bathymetry of the southwest part of Cain Dome (location in Figure 1). Explanation as in Figure 2. Jason 112 dive track (white) is superimposed. The basement is strongly affected by mass wasting in the southwestern part of the area. Jason samples indicate that basement is serpentinized harzburgite, often with associated gabbro or gabbro veins.

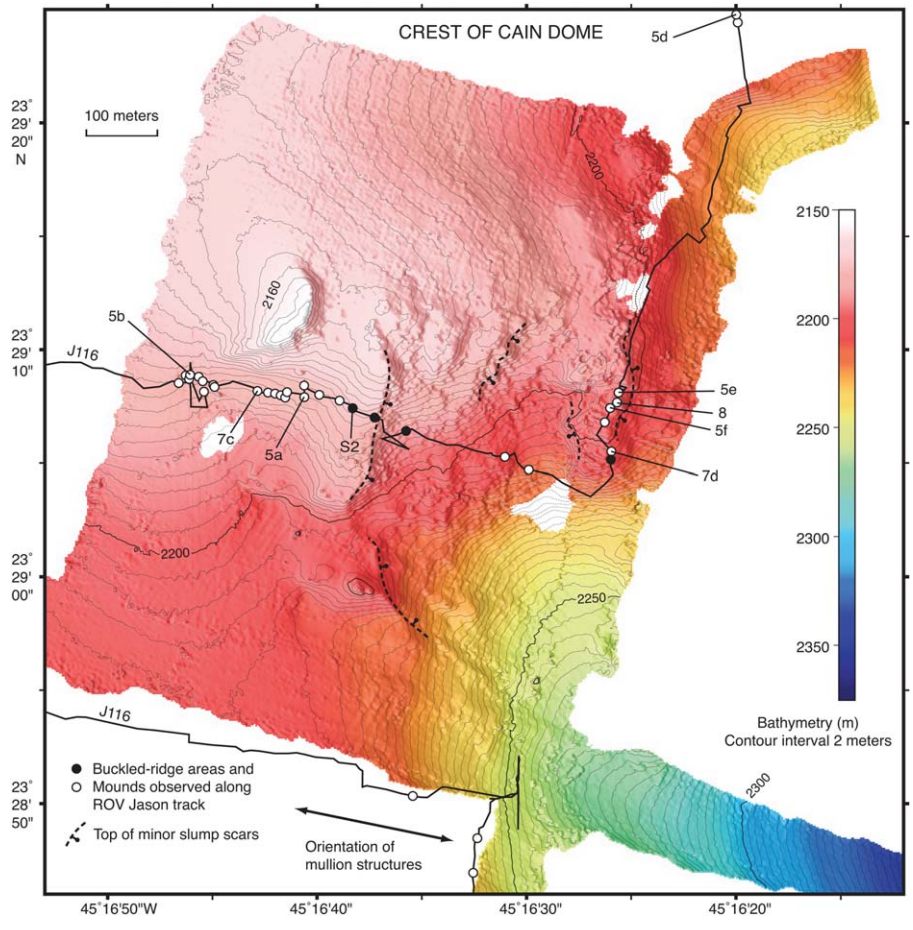

Figure 4. Shaded-relief map showing ABE Dive 146 multibeam bathymetry of the central part of Cain Dome (location in Figure 1). Explanation as in Figure 2, with filled circles showing areas of buckled ridges. Track of part of Jason Dive 116 (black line) is superimposed.

selected for detailed shorelab X-ray diffraction (XRD), petrographic, and geochemical analysis (Table 1). Mineral identifications and textural interpretations were made by XRD and from polished thin sections (transmitted and reflected light). Geochemical analyses of representative bulk samples and subsamples were performed by Activation Laboratories Ltd. (ACTLAB) in Ontario using inductively coupled plasma emission spectroscopy (ICP-ES) for the major elements and for V, Sr, and Ba, and using ICP mass spectrometry (ICP-MS) for the remaining trace and rare earth elements (REEs).

4. Morphology, Distribution, and Composition of Mounds

[17] Geological features that we interpret to be related to hydrothermal activity appear on all Jason dives that traversed the detachment-fault surface. The most common are large, prominent mounds consisting of igneous rock debris, cemented breccia, Fe-Mn-rich sediments, and chalks. Surfaces of the mounds vary from irregular, nearly pure igneous rock debris to primarily chalk. The chalks can form smooth pavements but they commonly are broken up or distorted. Ridges consisting of rock debris are also present; they are morphologically similar to mounds except that they extend for tens to hundreds of meters.

4.1. Igneous Rock Debris Mounds

[18] Among mounds that consist primarily of igneous rock debris, the smallest are simple rock clusters, sometimes with the debris moderately dispersed. These mounds are less than a meter high and up to a few meters in breadth. Their true scale and coherence are difficult to establish because they are mostly covered by sediments.

[19] In contrast, numerous large and well-defined rock mounds rise ~1–6 m above the surrounding

Table 1. Samples Analyzed for Mineralogy and Geochemistry

Sample Number	Description	Comment
Mound Samples		
J112-54	Lithified Fe-oxyhydroxide (goethite) with minor X-ray amorphous silica	From lower part of buckled ridge on top of a mound, southwest Cain Dome (Figures 9 and 13a–13d)
J112-98[a]	Serpentinized harzburgite breccia cemented by chalk with birnessite	From interior of chalk-paved mound, southwest Cain Dome (Figure 7e)
J112-104	Basalt breccia with birnessite matrix	From highly cemented, protruding core of a mound, southwest Cain Dome (Figures 7b and 11f)
J116-24[b]	Basalt-serpentinite breccia with quartz-chlorite matrix	From breccia boulder (apparent resistant mound core), central Cain Dome (Figure S1)
J116-30[a]	Polymict breccia with layered Mn oxide and Fe oxyhydroxide, and chalk	From elongate, low-relief mound (upper right in Figure 6e) adjacent to buckled ridges, central Cain Dome
J116-46	Layered Mn oxide (birnessite, minor todorokite) and Fe oxyhydroxide, and chalk	Broken from lineated boulder on lower part of a mound, central Cain Dome (Figures 10 and 12a)
Non-mound Samples		
KN180-2-16–18	Layered Mn oxide (birnessite, minor todorokite) and Fe oxyhydroxide, and chalk	Dredge sample from detachment surface on southeast Cain Dome (Figures 11a and 12c)
KN180-2-16–20	Layered Mn oxide (birnessite, minor todorokite) and Fe oxyhydroxide (goethite), and chalk	Dredge sample from detachment surface on southeast Cain Dome (Figures 11b and 12d)
J112-75	Lithified Fe-oxyhydroxide (goethite) with minor X-ray amorphous silica	Talus from large slump scar on southwest Cain Dome (Figures 11c and 13e, 13f)
J112-95	Layered Mn oxides (birnessite, minor todorokite) and Fe oxyhydroxide (goethite), and chalk	Talus (Figures 11e and 12b, 12e, 12f) from just below base of layered chalk outcrop shown in Figure S3a, southwest Cain Dome
J112-96	Chalk with Mn oxide and Fe oxyhydroxide (goethite) layers	Talus (Figure 11d) from just below base of layered chalk outcrop (Figure S3a), southwest Cain Dome
J112-97[a]	Layered Mn oxides (birnessite, todorokite) and Fe oxyhydroxide (goethite), and chalk	Talus from just below base of layered chalk outcrop, southwest Cain Dome (Figure S3)

[a]Mineralogy only (XRD and thin-section petrography).
[b]Geochemical analysis of outer crust only.

sediments. Surfaces of these mounds expose well-cemented igneous rock debris that has only a thin coating of unconsolidated sediment (Figures 5a–5c). The mounds typically have subconical to rounded profiles, widths about 3–4 times height, plan-view shapes that are circular to oval, and side slopes of 30°–50°. Constituent rocks are usually 10–20 cm or less in longest dimension but many reach 50–60 cm; larger rocks are much less common. Clasts are generally subangular and are mostly fragments of pillow basalt and basalt breccia. Smaller amounts of other rock types are present. Of 23 igneous rocks collected by ROV Jason from mounds, 11 are basalts, 4 are basaltic breccias, 5 are harzburgites, 1 is metagabbro, 1 is olivine gabbro, and 1 is soapstone (supporting information, Table S1).[1]

[20] Internal structure of some rock mounds is visible where part of the flank has failed (e.g., right side of Figure 5b). The mound interiors contain tightly packed, well-cemented clasts that appear to be igneous rock, based on angularity and samples collected. Interstices are filled with calcareous sediments and/or Fe-Mn and carbonate cements, resulting in low overall porosity.

4.2. Mounds With a Significant Chalk Component

[21] Mounds with large amounts of chalk have shapes similar to the igneous rock mounds but are more abundant and appear to attain larger sizes (up to ~8–10 m high). Some mounds have a relatively smooth surface that consists of chalk pavement (Figures 5f, 6a, and 6b). More commonly, the surfaces are somewhat irregular, incorporating subrounded chalk clasts, boulders, and slabs (Figures 5d and 5e). This debris can be difficult to distinguish from igneous rock in Jason video, although it is generally more rounded or slab-like. Fracturing, erosion, and mass wasting of the chalks suggest that most of these mounds originally had relatively complete chalk cover that has degraded over time.

[22] Disruption of the chalk cover is primarily in two forms. Most common are pancake-like slabs that have narrow intervening fissures but in aggregate create a relatively smooth surface (Figures 5f

[1]Additional supporting information may be found in the online version of this article.

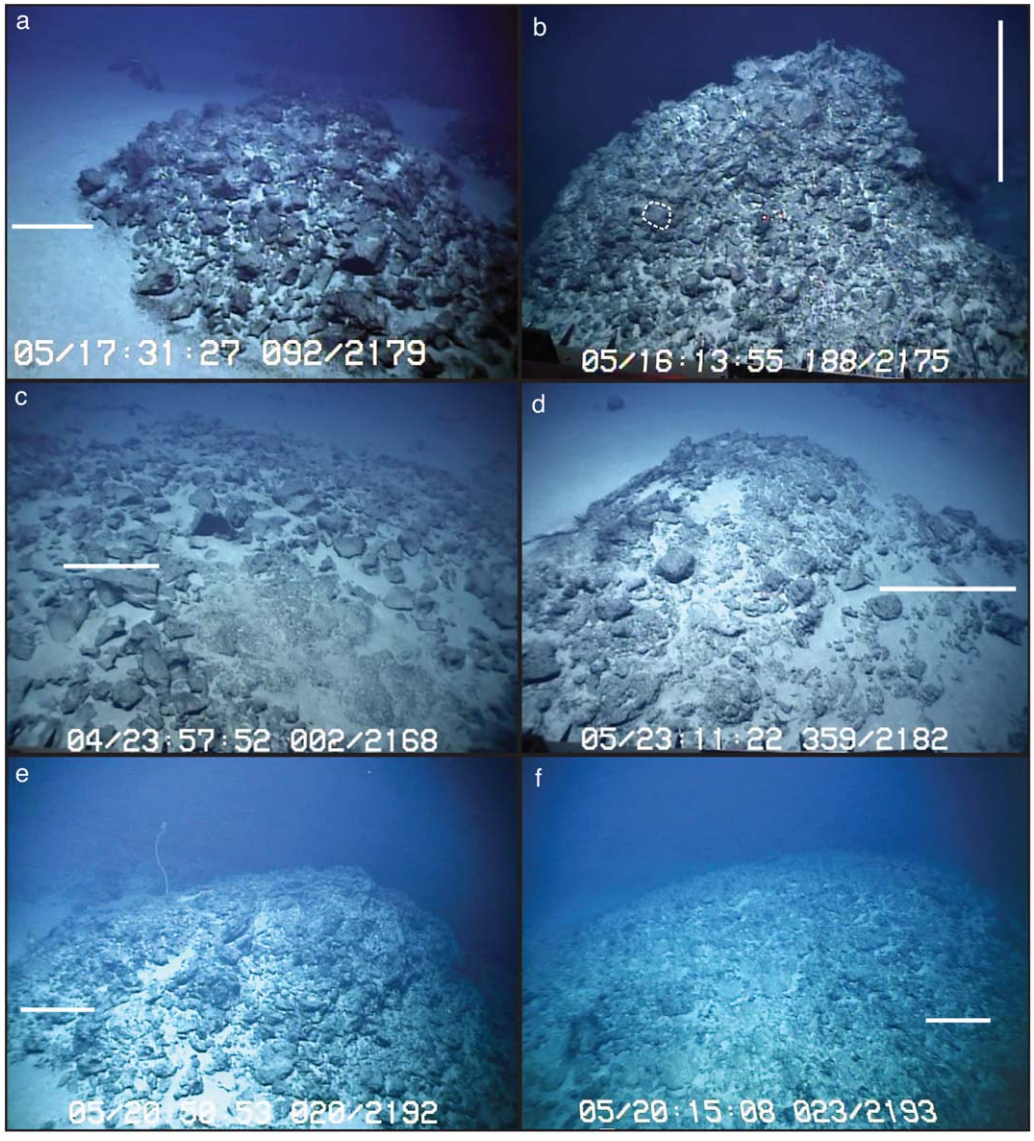

Figure 5. Frame captures from ROV Jason Dive 116 video on central Cain Dome showing mound surficial morphology that ranges from pure igneous rock debris (top) to mixed igneous rock and chalk slabs (bottom). Scale bars are 1 m at indicated depth in field. Code at bottom of frames is: day/time, heading/depth in meters. Mound locations (except 5c) are shown in Figure 4. (a) Very rounded mound of cemented igneous rock debris. Sample J116-41 from near the top of this mound is plagioclase olivine basalt. The mound is >2 m high and 5–6 m in long dimension. (b) Upper part of a mound consisting of a core of coarse igneous rock breccia with rather uniform clast size averaging 10–15 cm. Overall, the mound is circular in plan view, ~3 m high, and ~7 m in diameter. Sample J116-39 (dotted polygon) is plagioclase olivine basalt. (c) View down the side of a huge mound at 23°27′55.5″N, 45°17′11.0″W. The mound is tens of meters across, with abundant igneous rock (and likely chalk) debris averaging tens of centimeters in size; in foreground, the mound has a chalk cap. Sample J116-22 taken from the mound is basalt. (d) Mound covered by subrounded debris, probably chalk; the mound is ~3 m high and 6–7 m in diameter. (e) Very large, rounded mound, ~4–5 m high and 8–9 m long. Rounded and subangular debris suggest that the surface is covered by chalk and igneous rock fragments, respectively. (f) Crest of a huge mound; video and ABE bathymetry indicate that the mound is ~6 m high and >25 m long. The domed surface is very smooth and is covered with plates of probable chalk.

and 6b). The original cover probably was continuous, but it has been fractured and erosion in the cracks has formed subrounded blocks at submeter to multimeter scales. The most continuous cover is usually on low-gradient tops of mounds, with much more broken and intermittent cover on the

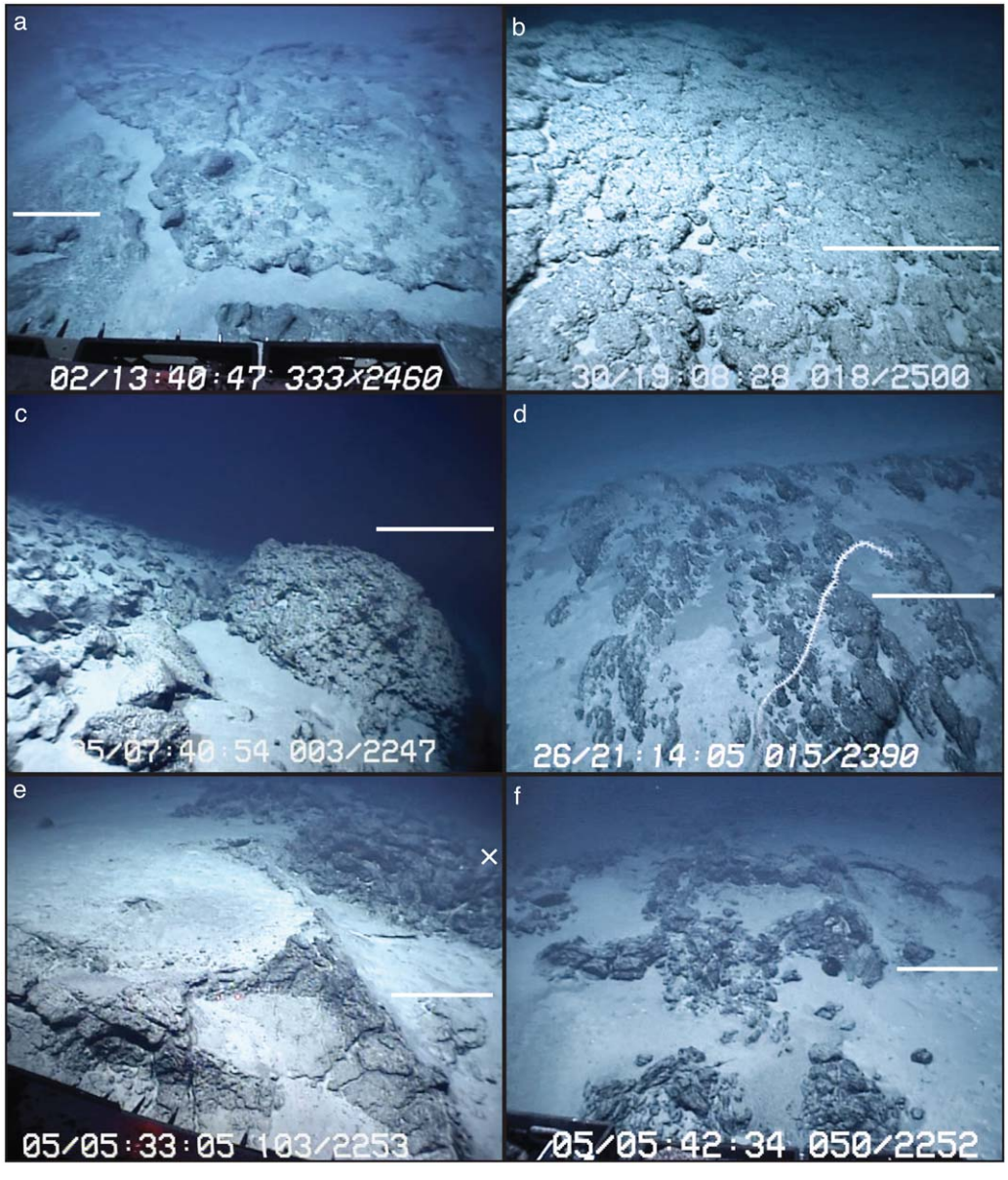

Figure 6. Frame captures from ROV Jason video showing morphology of mounds and chalks on the detachment surface. Explanation as in Figure 5 except that scale bar is 0.5 m in Figure 6e. Locations of Figures 6a, 6b, and 6d are shown in Figures 2 and 3. (a) Crest of very large mound, capped by lumpy chalk that is split by fissures (southeast Abel Dome, Jason Dive 114). (b) Crest and flank of very large mound on southeast Abel Dome, surfaced by chalk that has fractured and eroded into pancake-like plates (Jason Dive 113). (c) Bulbous "ball" likely composed of igneous rock breccia cemented by carbonate and hydrothermal precipitates, on a mound of igneous rock debris (central Cain Dome; Jason Dive 116, 23°28′39.5″N, 45°16′32.9″W). (d) Layered chalk that has been turned on edge, probably by downslope sliding of the sedimentary cover, and eroded (southwest Cain Dome, Jason Dive 112). (e) Buckled ridges forming polygonal patterns on central Cain Dome, with elongated mound at upper right (Jason Dive 116, 23°28′27″N, 45°16′35.5″W). Attempted sampling revealed that the ridges have a red-orange brown interior (i.e., they are enriched in Mn oxides and Fe oxyhydroxides) similar to other areas of buckled ridges (Figure 9; supporting information, Figure S2). Sample J116-30 taken at location X on the mound at upper right is a polymict breccia with layered Fe-Mn minerals and chalk. (f) Another aspect of buckled ridges in polygonal patterns, a few meters northwest of the location in Figure 6e. Here the ridges have highly contorted, ropey structure.

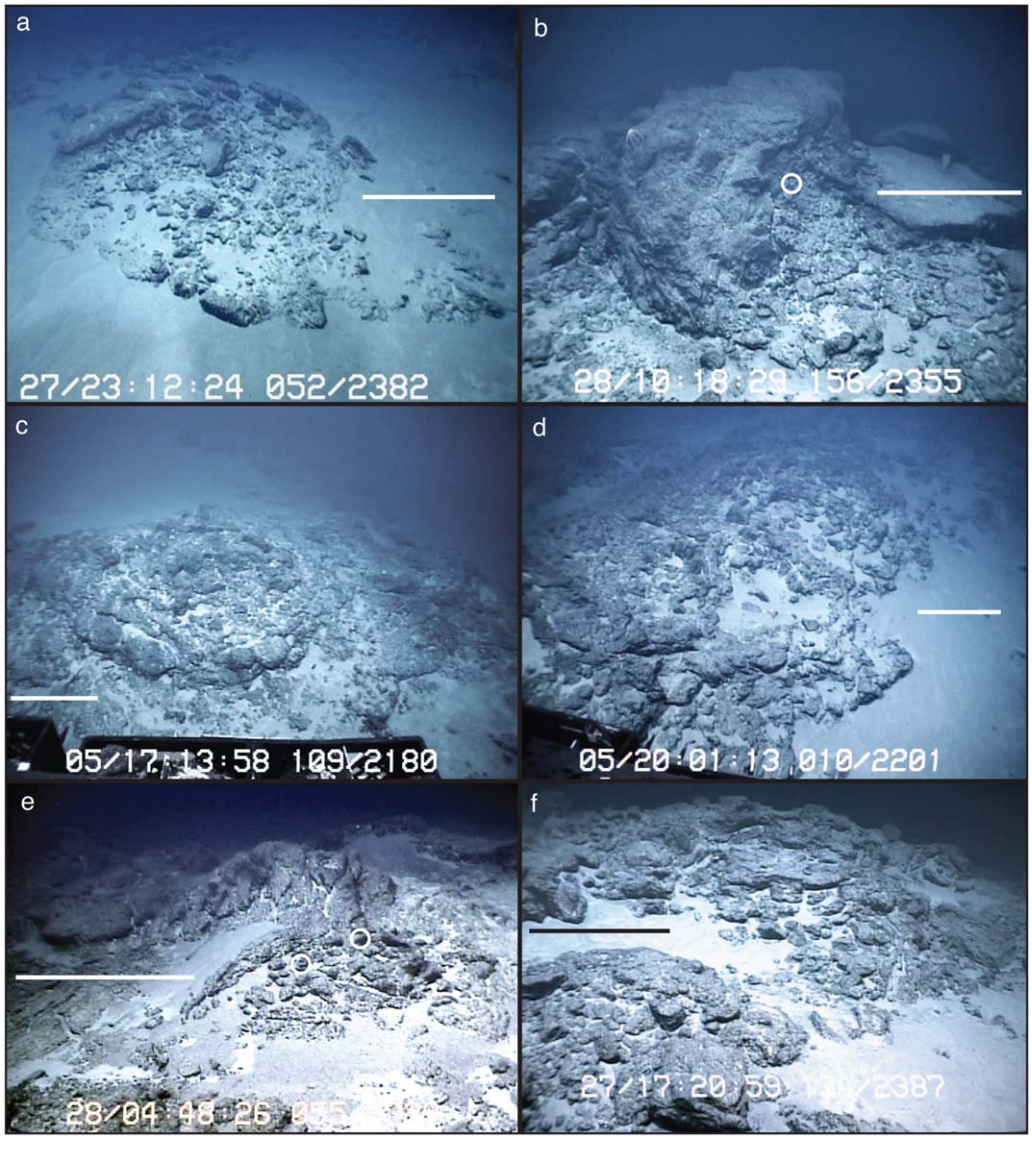

Figure 7. Frame captures from ROV Jason video (a,b,e,f—Dive 112, southwest Cain Dome; c,d—Dive 116, central Cain Dome) showing mound morphologies. Explanation as in Figure 5. Mound locations are shown in Figures 3 and 4. (a) Eroded mound, ca. 3 m in diameter, partially capped by relict slabs of chalk. (b) Elevated protrusion, consisting of breccia, at the top of a large mound partially covered by slabs of chalk in its lower reaches. Sample J112-104, indicated by circle, is basalt breccia with birnessite matrix. (c) Mound covered by contorted slabs of chalk in a quasi-annular pattern; overall diameter of the mound is ~8 m. (d) Mounded mass of highly contorted and fractured chalk (and likely breccia) forming part of a ~N-S trending ridge; three quasi-annular features ca. 1.5 m in diameter are present at the center of the frame. (e) Eroded mound that was originally capped by slab-like chalk; the interior also appears to contain chalk that cements a diverse assemblage of igneous rock debris. Circles show locations of samples J112-99 (left, olivine gabbro with harzburgite xenoliths) and J112-98 (right, serpentinized harzburgite breccia). (f) Crest area of a large (>7 m diameter) mound. Erosion of the chalk cap has exposed its ropey, contorted structure.

steeper flanks. Some mounds have a slightly depressed area near their crest that may be filled with unconsolidated sediment. A less common form of chalk cover consists of relatively continuous pavement that has been split by large (>10s of cm) fissures (Figure 6a). Like the cover noted above, this form occurs on low-gradient crests of mounds.

[23] Other mounds appear to consist almost entirely of contorted, lumpy chalk that produces an irregular surface (Figures 7c, 7d, and 7f). Exposures created by sampling attempts suggest that internal structure is similarly contorted. Part of the surface roughness is due to erosion, but it appears that the chalks have always had an irregular structure and the mounds were never covered by smooth chalk pavement. In places, the contorted chalk forms slightly elevated, quasi-annular structures around central depressions (Figures 7c and 7d).

[24] Mass wasting has exposed the interior of a number of these mounds. Internal composition ranges from predominantly igneous rock boulders and cobbles (Figure 7a) to a combination of igneous rock debris and layered chalk (Figure 7e). Chalk slabs with a "shingled" appearance occur around the lower parts of some degraded mounds; these may result from erosion of layered, internal chalks.

[25] Flank failure of one very large mound shows internal structure with clear bedding and flattened clasts (Figure 8). Apparent dip of the bedding is ~35° to the northwest. We made numerous attempts to sample clasts in this outcrop, but the samples crushed in the manipulator, revealing chalk with a white to yellow or yellow-brown interior. Thus, it appears that most of the flattened clasts in this outcrop are chalks. One successful sampling attempt (Jason sample J116-43) recovered soapstone consisting of a sheared lenticular phacoid of talc schist pseudomorphing peridotite. This soapstone is typical of those found along the damage zone of the detachment fault [*Dick et al.*, 2008].

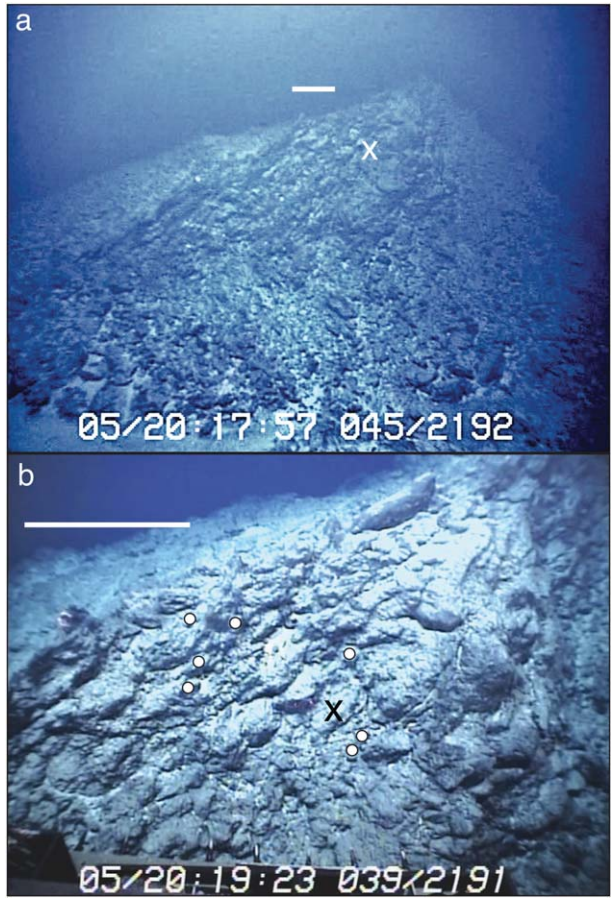

Figure 8. Frame captures from ROV Jason Dive 116 video of a huge (~9–10 m high), eroded and peaked mound on central Cain Dome. Explanation as in Figure 5. Mound location is shown in Figure 4. (a) Distant view of the mound, showing inclined layering with an apparent dip of ~35° to the northwest. (b) Close-up view of layering in the mound. Numerous sampling attempts (dots) show that the subrounded clasts are mostly chalk with yellow-brown interiors. The X in Figures 8a and 8b shows location of sample J116-43, which is soapstone.

4.3. Other Mound Features

[26] Near their crest, some mounds have steep-sided prominences or large boulders that are ~1–3 m high and consist of cemented rubble (Figures 5b and 7b; supporting information, Figure S1). We infer that these features are strongly cemented, erosion-resistant cores of mounds. The surrounding, lower parts of the mounds may or may not have slabs and other clasts of chalk present. Samples of the cores are polymict breccias and cobbles primarily of basalt but also peridotite and gabbro, all cemented together by carbonates (Figure S1) and/or Fe-Mn minerals (Figure 7b).

[27] Possibly related features are large cemented "balls" ca. 1–2 m in size (Figure 6c). Some balls are on mounds, but they also appear on the otherwise featureless detachment surface where they are surrounded by current-swept moats in unconsolidated sediment. They were not sampled but they exhibit irregular, pitted surfaces that suggest a breccia composition, probably with variable amounts of chalk.

4.4. Mound Distribution

[28] The detachment surface across Kane Megamullion is commonly disrupted by both major and minor slumping. We observed no mounds within areas of major slump scars (Figures 2 and 3) but some mounds are present in areas of apparently minor slumps (Figure 4, center). Thus, mounds appear to be associated with the original

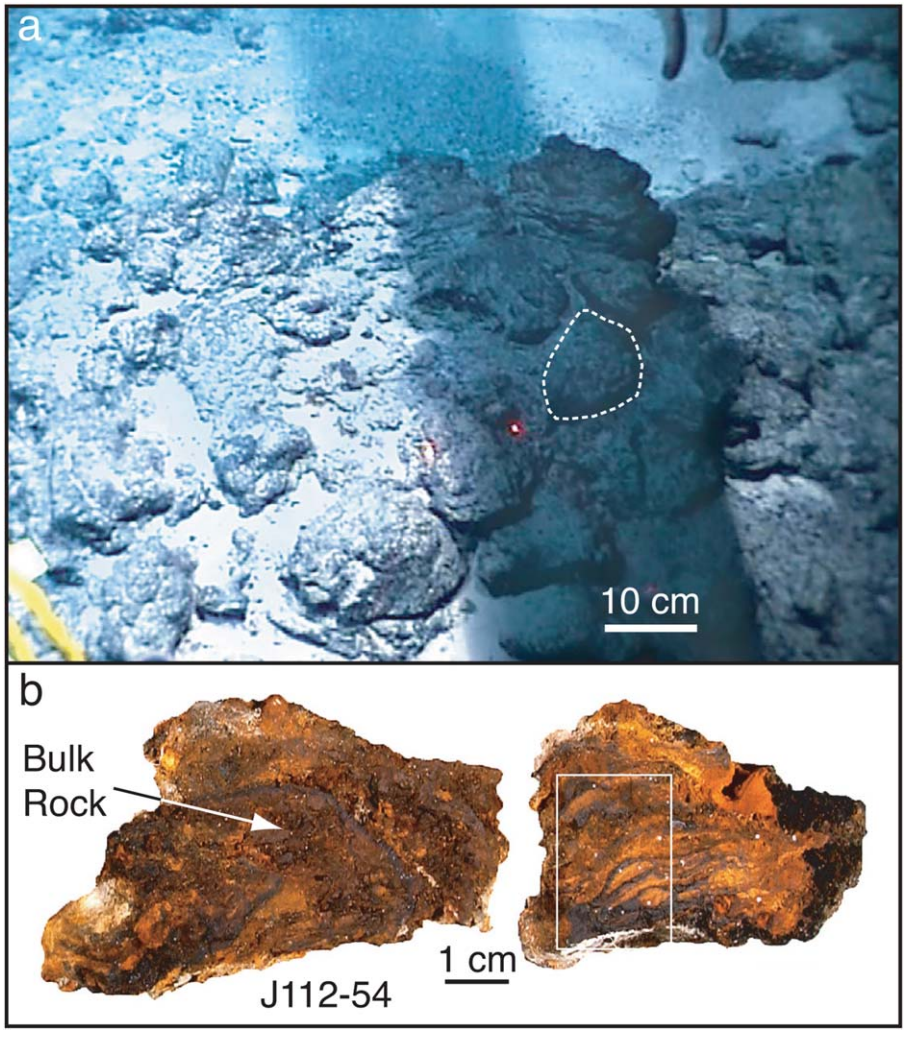

Figure 9. Deformed, Fe-Mn-rich sediments forming buckled ridges on top of a rubbley mound, southwestern Cain Dome, 2453m, Jason Dive 112. Location in Figure 3. (a) The ridges show outcropping layers in their upper part and form a quasi-annular pattern around a depression (in background) filled with light, unconsolidated sediment. (b) Sample J112-54, located by the dashed polygon in Figure 9a, exhibits interbedded and strongly distorted Fe-rich goethite layers. Arrow shows location of bulk geochemical sample and white rectangle locates thin section in Figures 13a–13d.

detachment surface. Mounds present in areas of major slumping probably have been destroyed, while mounds transported only short distances on minor slumps may have survived.

[29] Jason dive tracks provide only a limited visual swath, but there is enough along-track information to show that the concentration and distribution of mounds on the undisturbed detachment surface are not uniform. In some places, numerous mounds are grouped in areas a few tens of meters across, while in other places only single mounds are present (Figures 2–4). Individual mounds or groups of mounds are separated by $<$100 m to several hundred meters along the dive tracks.

4.5. Indications of Hydrothermal Activity at Mounds

[30] Samples from five mounds provide direct evidence of hydrothermal activity (see Table 1 and sections 6 and 7). One mound sampled during Jason Dive 112 (Figure 7b) on southwestern Cain Dome exhibits a protruding core $\sim$2.5 m high, with variable amounts of chalk lower on the mound flanks. Numerous sampling attempts show that the core is strongly cemented igneous rock debris with no evidence of chalk. The one sample obtained (J112-104, see Figure 11f) is a basalt breccia with birnessite (a hydrous Mn oxide)

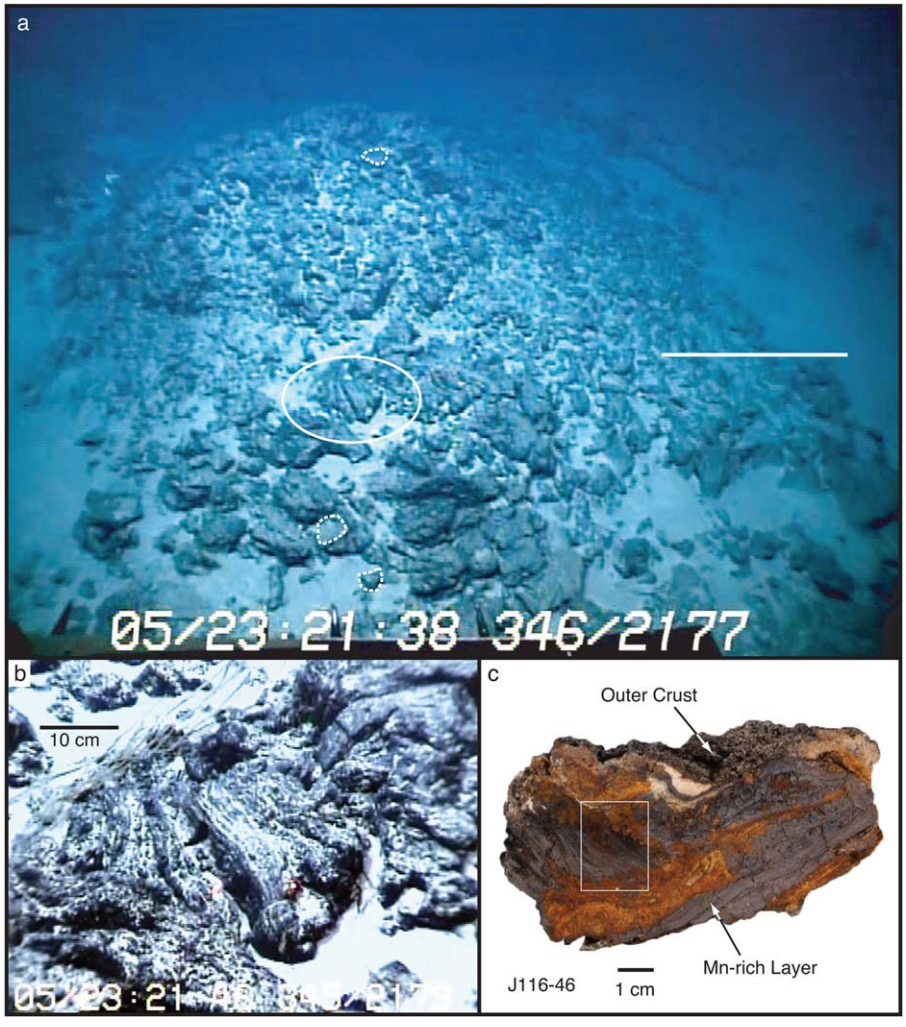

Figure 10. Mound near the northern crest of Cain Dome, Jason Dive 116 (23°29′26.2″N, 45°16′19.9″W). (a) Overview of mound, which consists of cemented, small igneous rock debris in its upper part, with hydrothermal Fe-Mn deposits and Fe-Mn-rich chalk in its lower part. Explanation as in Figure 5. Three dotted polygons show locations of samples J116-45 (bottom), J116-46 (center), and J116-47 and J116-48 (top). (b) Close-up view of lineated or layered structure in lower part of mound at location circled in Figure 10a. Wavy strands in the upper left part of the image are fronds of a sea pen. (c) Sample J116-46 from the lower part of the mound consists of contorted Mn oxides including birnessite (gray), Fe oxyhydroxides, and minor chalk. Arrows show locations sampled for geochemical analysis and white rectangle locates thin section in Figure 12a.

matrix that appears to be the primary cement in the mound core.

[31] Another mound sampled during Jason Dive 112 is covered by rubble with mostly subrounded shapes characteristic of chalks. At its crest are several contorted outcrops of chalk (Figure 9a), one of which is layered in its upper part and surrounds a pit filled with light, unconsolidated sediment. Attempted sampling showed that the layers have a yellow-brown interior, and sample J112-54 recovered from immediately below the layers consists of contorted, interbedded carbonates and lithified Fe oxyhydroxides (goethite) (Figure 9b).

[32] Three mounds sampled during Jason Dive 116 show evidence of hydrothermal activity. Sample J116-24 taken from a protruding boulder (possible core) of one mound is a basalt-serpentinite breccia with a quartz-chlorite matrix indicative of high-temperature hydrothermal alteration (Figure S1). Jason sample J116-30, consisting of layered Mn oxides, Fe oxyhydroxides, and carbonates in a polymict breccia, was obtained from rubble in a poorly developed mound that has an elongate, irregular shape and relatively low relief (Figure 6e). Debris in this mound ranges from subangular to subrounded; the Jason sample appears to be

typical of the latter form, which commonly exhibits contorted structure on its surface. A third mound (Figure 10a) has subangular rubble that averages 10–20 cm in size in its upper part where sampling recovered plagioclase olivine basalts (samples J116-47 and J116-48). The lower flanks of this mound exhibit larger, subrounded slabs and blocks, some of which show lineated surface structure (Figure 10b); it is unclear whether this is exposed internal layering or possibly represents flow structure. Sampling attempts showed that the slabs are well cemented and difficult to break apart but that samples could be crushed in the manipulator once freed from the outcrop. Two samples of this material, J116-45 and J116-46 (Figures 10a and 10c), consist of layered hydrothermal Fe-Mn precipitates and chalk.

4.6. Debris Fences and Ridges

[33] In some places on the detachment surface, notably on Jason Dives 116 and 117, there are long, relatively low-relief "fences" and high-relief ridges of rock debris. These features range from a few meters to more than 10 m wide with corresponding heights of <1 m to several meters, and they extend for tens to probably more than a hundred meters in length. They mostly are oriented roughly parallel or orthogonal to the direction of fault dip and their trends can be irregular, sinuous, or relatively linear. Huge ridges on the east flank of Adam Dome (Jason Dive 117; Figure 1) are up to $\sim$4 m high, generally have a rounded cross section, appear to be relatively linear, and are orthogonal to fault dip. All these features are largely igneous rock debris up to a few tens of centimeters in size, but some incorporate cobbles, slabs, or irregular cover of chalk, much like the mounds described earlier. Unlike the mounds, however, it is unclear whether their formation is related to hydrothermal activity.

5. Related Indications of Hydrothermal Venting

5.1. Buckled Ridges in Chalks

[34] In a number of areas, otherwise flat-lying chalks on the detachment surface are buckled into ridges generally less than a meter high and with a roughly triangular cross section (Figures 4 and 6e). Other buckled ridges are more disrupted, presenting an irregular, cobble-like appearance but with layering evident in individual blocks (Figure 6f). Some ridges form polygonal patterns with intervening cup-like depressions, but in other places they are relatively linear or wander irregularly. Internal structure of the ridges is strongly contorted (Figure 9; supporting information, Figure S2). Sample J112-54 from one of these ridges atop a mound (Figure 9) consists of irregular laminae of Fe oxyhydroxide (goethite). Other attempts to sample the ridges were unsuccessful because samples crushed in the manipulator, but broken surfaces revealed that the chalks have hues of yellow, brown, orange, red, and black that indicate Fe-Mn enrichment (Figure S2). Compared to hydrogeneous Fe-Mn crusts that are 5–10 mm thick on most igneous rocks sampled from the detachment surface, the contorted sediments commonly have only thin Fe-Mn veneers, suggesting that they are not static, fossil features. In rare instances, the chalk shows a fresh, naturally exposed surface (Figure S2b) that suggests internal disturbance.

5.2. Other Chalks

[35] Slumping, sliding, and other deformation has exposed cross sections of chalk cover on parts of the detachment surface (Figure 6d; supporting information, Figure S3). Some of these sections show pronounced, often contorted layers of well-cemented, resistant horizons interleaved with more erosion-prone layers. Samples from immediately below one of these outcrops (Figures 11d, 11e, and S3) contain Fe-Mn-rich layers that indicate hydrothermal precipitation and alteration/replacement of chalks. Similar samples occur in dredges from southeast Cain Dome (Figures 11a and 11b) and from talus in a slump scar on southwestern Cain Dome (Figure 11c) but the specific geological context of these samples is unknown.

[36] Elsewhere, Jason and dredge samples of chalk lack significant layering and distortion of bedding and show no clear indications of hydrothermal activity. One notable exception is dredge KN180-2-28 from the detachment surface on Adam Dome (Figure 1). Although chalks in this dredge show no sign of Fe-Mn enrichment, they contain numerous specimens (mostly fragmentary) of large gastropods that are interpreted to have been associated with high-temperature hydrothermal venting [*Kaim et al*., 2012]. Isolation of these specimens in otherwise "nonhydrothermal" sediments suggests that the geologic record of vent precipitates can be extremely localized.

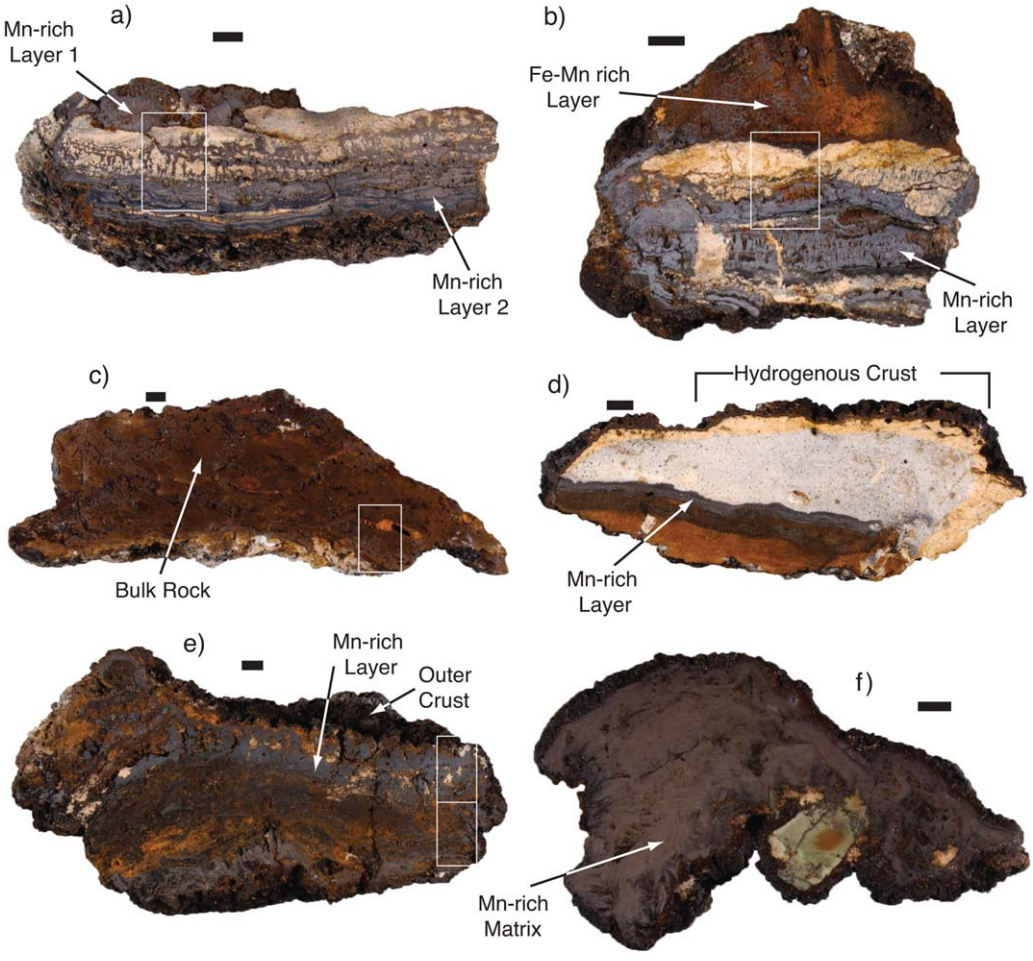

Figure 11. Photos of a subset of samples analyzed for geochemistry; sample locations in Figures 1 and 3. (a) Dredge sample KN180-2-16–18 and (b) KN180-2-16–20, layered Fe-Mn minerals and chalk from southeast Cain Dome. (c) Sample J112-75, lithified Fe-oxyhydroxide (goethite); talus from slump scar on southwest Cain Dome. (d) Sample J112-96, chalk and layered Fe-Mn minerals; talus from southwest Cain Dome. (e) Sample J112-95, crudely layered Fe-Mn minerals with minor carbonate; talus from southwest Cain Dome. (f) Sample J112-104, basalt breccia with birnessite matrix, from the core of a mound on southwest Cain Dome (Figure 7b). Scale bars are 1 cm. Arrows show locations sampled for geochemical analysis and white rectangles locate thin sections in Figures 12 and 13.

6. Sample Mineralogy

[37] We examined 12 samples in thin sections and by XRD (Table 1). The samples are of two major types: (1) chalks from both mounds and layered sediments on the detachment surface that are associated with, and in at least some cases are partially or totally replaced by, hydrothermal Fe-Mn precipitates, and (2) hydrothermally altered breccias from mounds. Most samples have a surficial Fe-Mn crust, typically 5–10 mm thick, on at least one surface. These crusts are consistently composed of δ-MnO_2 that is intergrown with amorphous Fe oxyhydroxides, typical of a hydrogenous origin.

6.1. Hydrothermal Mn Oxides and Fe Oxyhydroxides Mineralizing Sediments

[38] All sediment samples have complex lithologies consisting of varying proportions of chalk and hydrothermal Fe-Mn precipitates and many show laminae that are strongly contorted (Figures 9–11 and S3). The chalk is 86–93% calcium carbonate consisting of calcareous microfossils and micrite. Layers of Fe-Mn mineralization vary in thickness from <1 cm to a few centimeters. They show a spectrum of mineralization types that range from layers of relatively pure Mn oxides to layers of relatively pure Fe oxyhydroxides, although most

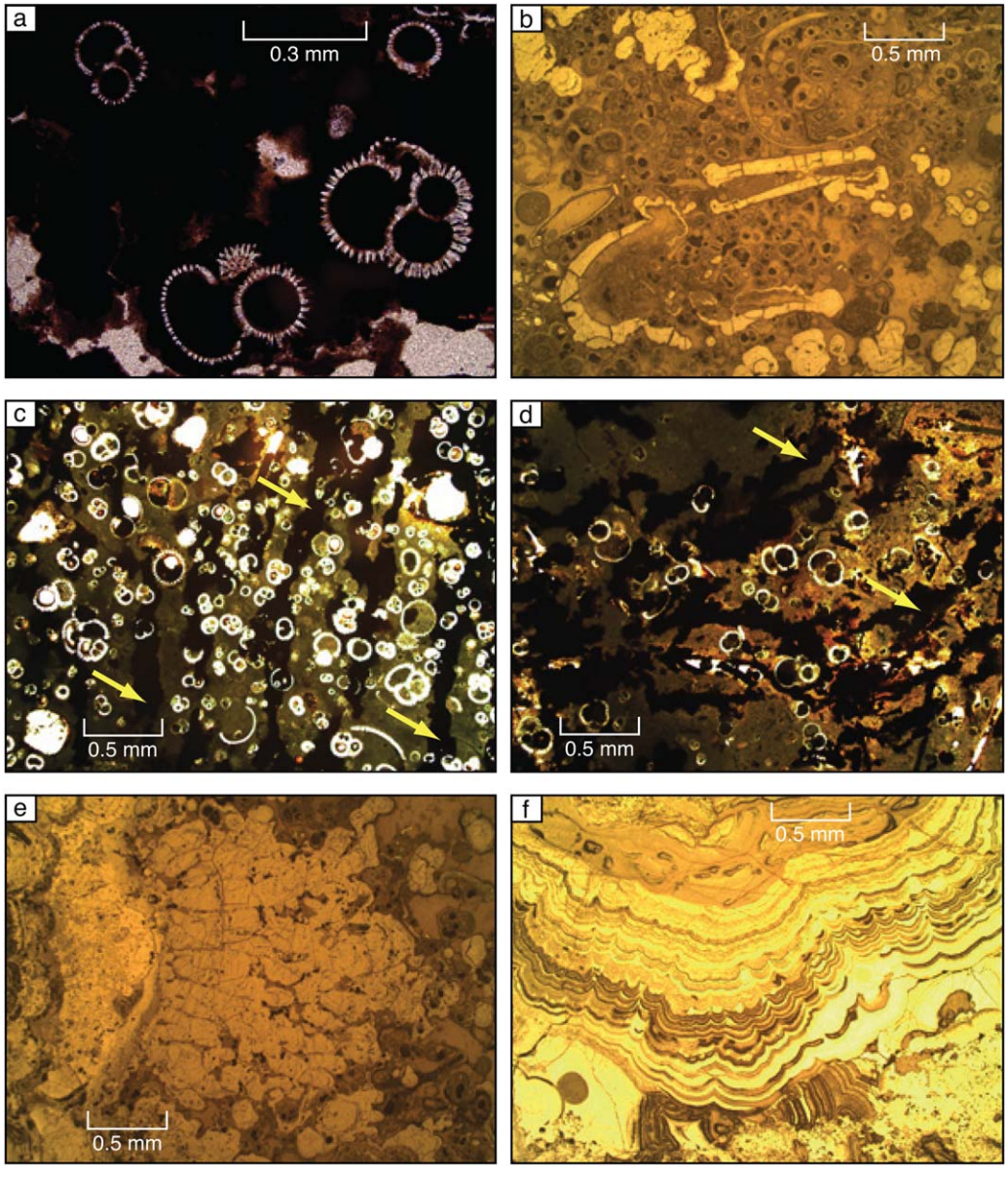

Figure 12. Photomicrographs of Mn-rich layers in samples from Kane Megamullion. (a) Planktonic foraminifera filled with Mn oxide; transmitted light, mound sample J116-46 (Figure 10). (b) Calcareous microfossils (light areas) totally replaced by Mn oxide; reflected light, crudely layered talus sample J112-95 (Figure 11e) from below outcrop in Figure S3a. (c, d) Microchannels (arrows show examples) filled with Mn oxide that also infills calcareous tests; transmitted light, layered samples (c) KN180-2-16–18 (Figure 11a) and (d) KN180-2-16–20 (Figure 11b). (e) Growth of Mn oxide emanating from colloform Mn oxide (left) and penetrating calcareous sediment (right); reflected light, sample J112-95. (f) Massive colloform todorokite in a Mn-rich layer; reflected light, sample J112-95.

samples show complex interlayering of both end members. For descriptive purposes, mineralization is divided into three types as discussed below.

6.1.1. Mn-Rich Mineralization

[39] There are two styles of Mn-rich mineralization: (1) pervasive filling of calcareous microfossils (e.g., sample J116-46, Figure 12a), and (2) massive stratabound layers either intercalated within unaltered chalks (e.g., sample KN180-2-16-18, Figure 11a) or almost totally mineralizing the chalk, typically with mixed laminae of Mn oxides and Fe oxyhydroxides (e.g., J112-95, Figures 11e, 12b, 12e, and 12f). Although the Mn-rich mineralization can be pervasive, some samples (e.g., KN180-2-16–18 and KN180-2-16-20, Figures 11a

and 11b) exhibit small microchannels of birnessite that cut across the chalk layers and infill foraminiferal tests within otherwise unaltered sediment (Figures 12c and 12d). Infilling of tests in the microchannels supports interpretation of the channels as pathways of fluid flow through the carbonate between stratabound Fe-Mn laminae, as opposed to formation by asicular growth. The latter may occur in sample J112-95, where Mn oxides grow in columns from colloform Mn oxide, penetrating and replacing the carbonate (Figure 12e).

[40] Stratabound layers of black, lustrous Mn oxides occur in many samples (e.g., J116-46, J112-97, KN180-2-16–18, KN180-2-16–20, and J112-95, Figures 10, 11, and S3). XRD analysis indicates that the major minerals in these layers are hydrous Mn oxides (birnessite and todorokite) in varying proportions. Individual layers up to 20 mm thick are massive and composed of ~2 mm-thick laminae. Well-developed colloform textures are common (Figure 12f), suggesting that the Mn oxides may have been deposited either on the seafloor or in open or water-rich spaces within the sediments.

6.1.2. Fe-Mn-Rich Mineralization

[41] Many of the samples exhibit complex, interlayered orange to dark brown laminae that vary from a few mm (e.g., sample J112-97, Figure S3) to >4 cm thick (e.g., KN180-2-16–20, Figure 11b). XRD analyses indicate that the laminae are goethite with todorokite and birnessite. The laminae are contorted and in many cases discontinuous, which suggests that they precipitated within the sediment rather than on the seafloor. Sample J112-96 (Figure 11d) shows particularly striking and sharply defined boundaries of goethite-rich (brown) and Mn-rich layers, with replacement indicated by microfossils that are partially dissolved.

6.1.3 Fe-Rich Mineralization

[42] Two samples (J112-54, Figure 9, and J112-75, Figure 11c) are distinguished by a composition that is almost entirely goethite with vuggy porosity. Sample J112-54 is yellow-brown with contorted, fine red-brown laminae up to ~0.4 mm thick (Figures 13a and 13b). Rare large vugs commonly are filled by late-stage Mn oxides that exhibit concentric growth patterns (Figure 13c). Evidence that hydrothermal fluids flowed through and deposited precipitates within sediments is observed in small, discrete patches where microfossils are filled with goethite (Figure 13d). Sample J112-75 is composed of more massive goethite with X-ray amorphous silica surrounding or filling vugs (Figures 13e and 13f).

6.2. Hydrothermally Altered Breccias

[43] Three samples from mounds are hydrothermally altered breccias that exhibit variations in both clast and matrix lithology. One sample (J112-104, Figures 7b and 11f) consists of small clasts of hydrothermally altered basalt in a matrix of birnessite that shows both asicular and colloform textures. The birnessite likely both precipitated in voids and replaced calcareous sediment, cementing the clasts and filling foraminiferal tests.

[44] Sample J112-98 (Figure 7e) is a large fragment of serpentinized harzburgite together with small basalt fragments cemented by chalk. Birnessite is present within the chalk, indicating that hydrothermal fluids percolated through the sediments and igneous rock clasts that comprise this mound.

[45] Sample J116-24 (Figure S1) contains large clasts of hydrothermally altered basalt and smaller clasts of serpentinite in a quartz-chlorite matrix. The mineralogy of this sample clearly indicates that it was part of a high-temperature hydrothermal system, probably at or near the ridge axis.

7. Sample Geochemistry

[46] Because of the complex layering and heterogeneity exhibited in many samples, we conducted most geochemical analyses on subsamples picked from specific layers to examine their origin. Two exceptions are samples J112-54 and J112-75 (Figures 9 and 11c) which are composed almost entirely of goethite; for these, we took bulk samples from the interiors. In sample J112-104 (Figures 7b and 11f), we separated a subsample of the birnessite matrix from the breccia. Finally, we separated black surficial Fe-Mn crusts from three samples for geochemical analyses: J112-95 (Figure 11e) and J116-46 (Figure 10), both of which consist of layered Fe-Mn minerals and chalk, and J116-24, the hydrothermally altered basalt-serpentinite breccia (Figure S1).

[47] Major, trace, and REE analyses are presented in Tables 2–4, respectively. Figure 14 shows a ternary diagram of Fe, Mn, and Co + Ni + Cu for the samples analyzed, and it clearly distinguishes

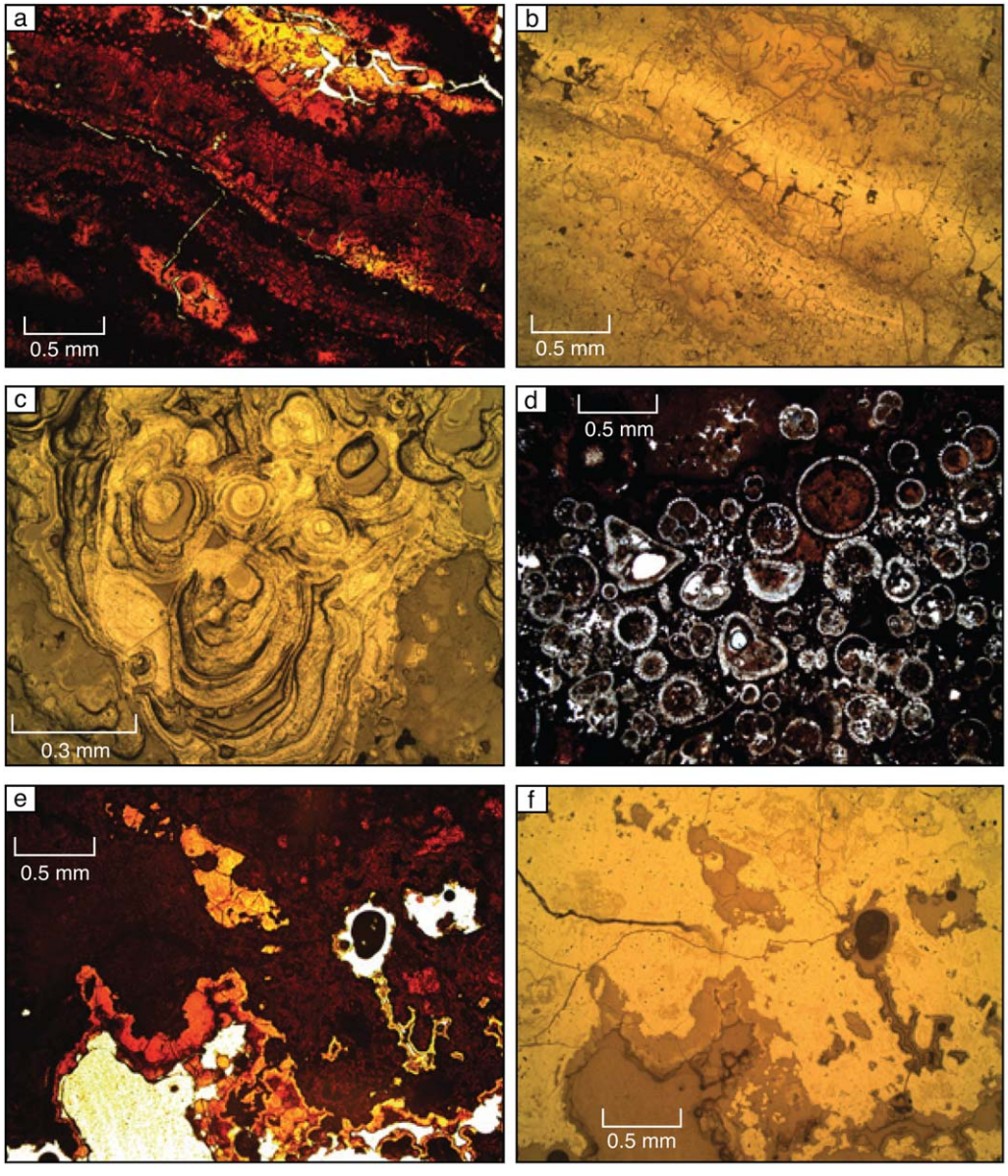

Figure 13. Photomicrographs of ironstones. (a, b) Light and dark brown banding of goethite in transmitted light (a) and reflected light (b) in layered, buckled sample J112-54 (Figure 9). (c) Concentric growth patterns of Mn oxides filling a large vug; reflected light, sample J112-54. (d) Foraminifera filled with goethite; transmitted light, sample J112-54. (e, f) Massive goethite with X-ray amorphous silica (light brown in Figure 11e) lining and infilling vugs; transmitted light (e) and reflected light (f) in vuggy, poorly layered talus sample J112-75 (Figure11c).

between hydrothermal and hydrogenous Fe-Mn precipitates. All the layered samples, together with the birnessite matrix in the J112-104 breccia, show a broad range in Fe versus Mn content but they fall in the hydrothermal field or are slightly enriched in the Co + Ni + Cu component. All the surficial Fe-Mn crusts analyzed have a hydrogenous origin.

7.1. Hydrothermal Mn Oxides and Fe Oxyhydroxides Mineralizing Sediments

7.1.1. Mn-Rich Mineralization

[48] The Mn-rich stratabound layers show a range in composition. Three of the layers (samples KN180-2-16-18 Layer 2, Figure 11a; KN180-2-16-20, Figure 11b; and J116-46, Figure 10) are

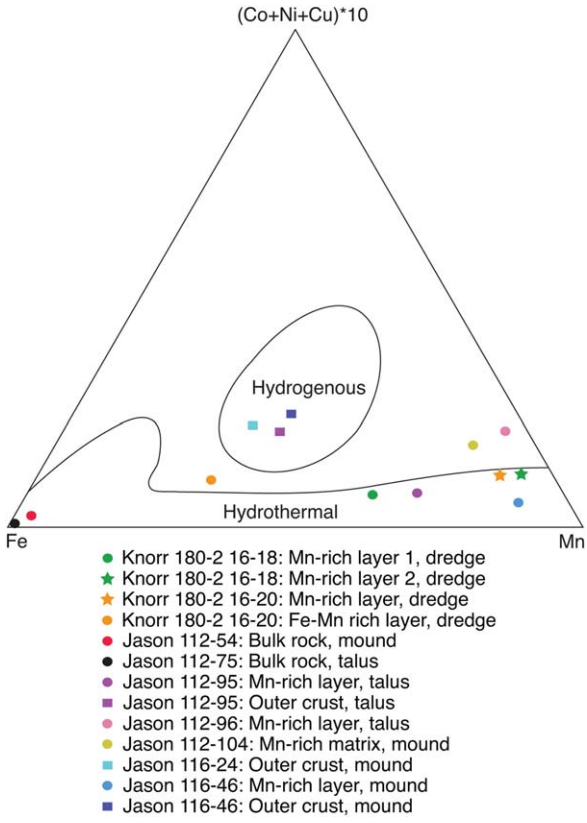

Figure 14. Ternary diagram illustrating the hydrothermal origin and range in composition of Mn oxides and Fe oxyhydroxides analyzed for geochemistry, as well as the hydrogenous origin of Fe-Mn surficial crusts. Labeled fields are defined by data from central Pacific hydrogenous crusts (after *Hein et al*., 1992) and data for hydrothermal samples from *Bonatti et al*. [1972], as reported in *Hein et al*. [2005].

relatively pure Mn oxides and are characterized by high Mn (33.3–40.3 wt.%) and very low Fe (1.7–3.9 wt.%) that results in Fe/Mn ratios of 0.05–0.11. The Mn-rich layer in sample J112-96 (Figure 11d) has the least Mn mineralization, as reflected by its CaO content of 27.2 wt.%, but it also has a low Fe/Mn ratio of 0.04 similar to the other Mn-rich layers. Two other Mn-rich layers (KN180-2-16-18 Layer 1, Figure 11a; J112-95, Figure 11e) are clearly mixed Mn oxides and Fe oxyhydroxides. While their Mn contents are only slightly lower (27.1 wt.% and 30.2 wt.%, respectively) than the other layers, their Fe contents are significantly higher (15.1 wt.% and 11.1 wt.%, respectively) resulting in Fe/Mn ratios of 0.56 and 0.37, respectively.

[49] *Toth* [1980] has suggested that Co/Zn ratios are a sensitive indicator of the source of trace metals. The Co/Zn ratios in the above six samples range from 0.08 to 0.62 (average 0.30), which is indicative of a hydrothermal origin of the trace metals [*Toth*, 1980]. The samples also contain high concentrations of Zn (460–950 ppm, excluding sample J112-96 which is diluted by $CaCO_3$) and Mo (all but one >100 ppm), which is characteristic of hydrothermal deposits [*Hein et al*., 1997].

[50] Total REE contents in these samples are low (12–125 ppm) and, except for sample J116-46, the chondrite-normalized REE patterns are all very similar, showing LREE enrichment and variable negative Ce anomalies (Figure 15a). This is typical of hydrothermal deposits and is within the range of REE patterns exhibited by ferromanganese deposits in the Alvin and low-temperature zones of the TAG hydrothermal field [*Mills et al*., 2001] and the Ashadze-1 hydrothermal field at 13°N on the MAR [*Davydov et al*., 2007]. Ce anomalies in hydrothermal deposits range from no anomaly to strongly negative depending on the amount of mixing with seawater and the rate of precipitation [*Hein et al*., 1997].

7.1.2. Fe-Mn-Rich Mineralization

[51] The stratabound layers form a continuum in chemistry from Fe-rich to Mn-rich. We analyzed

Table 2. Major Element Concentrations (in wt.%) in Bulk Rock and Layers in Dredge and Jason Samples From Kane Megamullion

Sample Number	Description	SiO_2	Al_2O_3	Fe_2O_3(T)	MnO	MgO	CaO	Na_2O	K_2O	TiO_2	P_2O_5	LOI
KN180-2-16-18	Mn-rich layer 1	1.67	0.86	21.54	34.99	4.08	2.49	2.93	0.78	0.025	0.56	26.82
	Mn-rich layer 2	2.11	2.45	2.48	43.03	5.67	5.08	2.57	1.19	0.094	0.07	28.88
KN180-2-16-20	Mn-rich layer	1.65	1.90	5.16	43.95	4.82	6.97	3.14	0.81	0.085	0.17	26.95
	Fe-Mn-rich layer	6.65	1.46	37.98	17.76	3.18	1.02	1.69	1.02	0.021	0.96	23.18
Jason 112-54[a]	Bulk rock	11.86	0.23	60.34	1.56	1.62	1.96	0.73	0.69	0.019	0.78	18.92
Jason 112-75	Bulk rock	10.25	0.03	72.85	0.15	1.51	0.53	0.30	0.57	<0.001	0.27	14.32
Jason 112-95	Mn-rich layer	6.58	1.74	15.87	39.03	2.78	1.96	1.59	1.48	0.116	0.27	22.43
	Outer crust	5.45	2.33	22.82	18.01	1.98	7.11	1.70	0.46	1.378	0.91	33.45
Jason 112-96	Mn-rich layer	3.73	1.79	1.19	25.24	2.37	27.24	0.15	0.04	0.089	0.06	32.44
Jason 112-104[a]	Mn-rich matrix	3.32	1.97	7.28	47.39	4.75	2.38	0.97	0.19	0.552	0.31	26.58
Jason 116-24[a]	Outer crust	8.79	3.37	27.58	17.19	2.45	3.88	1.16	0.27	2.06	1.09	33.12
Jason 116-46[a]	Mn-rich layer	2.40	0.55	5.68	52.11	4.06	6.35	1.64	0.09	0.015	0.15	25.36
	Outer crust	4.54	1.97	23.69	20.85	2.50	5.94	2.16	0.54	1.101	0.92	32.54

[a]Samples from mounds.

Table 3. Trace Element Concentrations (in ppm) in Bulk Rock and Layers in Dredge and Jason Samples From Kane Megamullion

Sample Number	Description	V	Cr	Co	Ni	Cu	Zn	As	Sr	Y	Zr	Mo	Ba	Pb	Th	U
KN180-2-16-18	Mn-rich layer 1	576	<20	39	1910	790	490	862	324	26.8	47	>100	440	<5	0.24	1.70
	Mn-rich layer 2	165	<20	300	3160	1150	950	47	388	25.1	25	56	373	12	1.54	0.88
KN180-2-16-20	Mn-rich layer	184	<20	100	3350	1460	950	153	427	21.4	34	>100	724	8	0.77	1.07
	Fe-Mn-rich layer	798	<20	43	2730	1540	820	966	241	41.8	110	>100	411	<5	0.31	2.82
Jason 112-54[a]	Bulk rock	433	<20	134	780	220	80	204	218	12.8	22	23	57	7	0.66	2.98
Jason 112-75	Bulk rock	25	<20	<1	70	<10	<30	24	67	6.6	6	10	12	<0.5	<0.05	0.37
Jason 112-95	Mn-rich layer	233	<20	126	700	2240	460	374	636	27.6	77	>100	2422	18	1.86	1.20
	Outer crust	736	20	5010	1230	720	400	532	1173	174	367	>100	971	675	55.6	9.16
Jason 112-96	Mn-rich layer	54	<20	106	2280	2450	280	23	720	15	41	>100	2951	13	1.59	0.97
Jason 112-104[a]	Mn-rich matrix	328	20	1760	4380	1970	1280	162	569	67.8	132	>100	656	25	15.4	3.26
Jason 116-24[a]	Outer crust	936	30	6640	1360	470	440	1070	1247	218	410	>100	937	1000	62.7	11.0
Jason 116-46[a]	Mn-rich layer	174	<20	323	1520	310	520	46	494	12	9	>100	487	<5	0.35	1.67
	Outer crust	768	<20	4380	4060	1010	820	919	1058	159	309	>100	672	697	53.1	8.46

[a]Samples from mounds.

one sample (KN180-2-16-20, Figure 11b) from an Fe-Mn-rich layer dominated by goethite with birnessite and minor todorokite. It contains 26.6 wt.% Fe and 13.7 wt.% Mn (Fe/Mn ratio = 1.9) and plots slightly toward the Fe-rich end of the range of hydrothermal deposits in the ternary diagram (Figure 14). Apart from Fe and Mn contents, its major and trace element chemistry does not differ significantly from the other stratabound layers, although it contains somewhat higher V and Zr, and lower Co concentrations. Its Co/Zn ratio is 0.05, indicative of a hydrothermal origin.

[52] The chondrite-normalized REE pattern of this sample (Figure 15a) falls within the same range as the more Mn-rich stratabound layers, although it exhibits a stronger negative Ce anomaly. This reflects either a more rapid rate of precipitation than the Mn-rich stratabound layers or a difference in the amount of mixing with seawater [*Hein et al*., 1997].

7.1.3. Fe-Rich Mineralization

[53] The two goethite samples (J112-54, Figure 9; J112-75, Figure 11c) are characterized by high Fe (42.2–50.9 wt.%) and low Mn (0.1–1.2 wt.%) concentrations and, with Mn/Fe ratios of <0.03, can be classified as ironstones. Their location at the iron apex of the ternary diagram (Figure 14) indicates extreme fractionation of Fe from Mn, the result of differing solubilities of their oxides during precipitation from hydrothermal fluids. These samples also contain significant X-ray amorphous silica (10–12 wt.%) that likely precipitated from the conductively cooling hydrothermal fluid or a hydrothermal fluid/seawater mix. The samples are similar to hydrothermal iron-oxide silica deposits found in a variety of tectonic settings including mid-ocean ridges and seamounts [e.g., *Boström and Widenfalk*, 1984; *De Carlo et al*., 1983; *Hein et al*., 1994; *Lalou et al*., 1977; *Mills and Elderfield*, 1995; *Puteanus et al*., 1991].

[54] Although they are similar in major-element composition, the two ironstone samples differ in trace element and REE concentrations. Both have generally lower concentrations of trace and REE elements than the other Fe-Mn mineralization types, but J112-54 has significantly higher concentrations of V, Co, Ni, Cu, Zn, and As than J112-75

Table 4. REE Concentrations (in ppm) in Bulk Rock and Layers in Dredge and Jason Samples From Kane Megamullion

Sample Number	Description	La	Ce	Pr	Nd	Sm	Eu	Gd	Tb	Dy	Ho	Er	Tm	Yb	Lu
KN180-2-16-18	Mn-rich layer 1	11.0	15.0	2.10	9.35	2.47	0.637	3.18	0.57	3.83	0.87	2.81	0.432	2.85	0.451
	Mn-rich layer 2	20.2	33.0	3.92	16.10	3.86	1.010	4.77	0.79	4.79	0.96	2.88	0.414	2.49	0.393
KN180-2-16-20	Mn-rich layer	15.5	18.8	2.48	9.91	2.36	0.658	3.15	0.52	3.31	0.70	2.17	0.325	2.05	0.319
	Fe-Mn-rich layer	22.3	11.5	3.82	15.50	3.89	1.050	5.19	0.85	5.73	1.31	4.31	0.723	5.07	0.765
Jason 112-54[a]	Bulk rock	6.44	13.4	1.51	5.87	1.33	0.356	1.46	0.23	1.42	0.33	1.03	0.148	0.92	0.144
Jason 112-75	Bulk rock	0.47	0.90	0.14	0.86	0.28	0.392	0.44	0.09	0.62	0.16	0.62	0.105	0.72	0.122
Jason 112-95	Mn-rich layer	29.2	46.6	5.43	20.80	4.49	1.160	4.99	0.76	4.57	0.92	2.79	0.405	2.45	0.363
	Outer crust	318.0	1130.0	63.70	239.00	55.40	13.500	51.30	7.87	44.70	8.55	24.90	3.530	21.00	2.960
Jason 112-96	Mn-rich layer	18.6	23.8	4.51	17.60	4.07	0.990	4.05	0.58	3.26	0.63	1.70	0.230	1.35	0.186
Jason 112-104[a]	Mn-rich matrix	106.0	358.0	24.20	89.70	20.40	4.960	19.20	3.03	17.60	3.45	9.61	1.320	7.97	1.160
Jason 116-24[a]	Outer crust	386.0	1310.0	77.80	299.00	70.90	17.000	65.20	10.00	56.60	11.00	31.40	4.380	26.70	3.810
Jason 116-46[a]	Mn-rich layer	2.16	4.27	0.47	1.71	0.40	0.119	0.48	0.08	0.52	0.16	0.56	0.086	0.56	0.077
	Outer crust	285.0	923.0	58.50	221.00	52.60	12.800	48.50	7.32	41.50	8.07	22.50	3.110	18.60	2.600

[a]Samples from mounds.

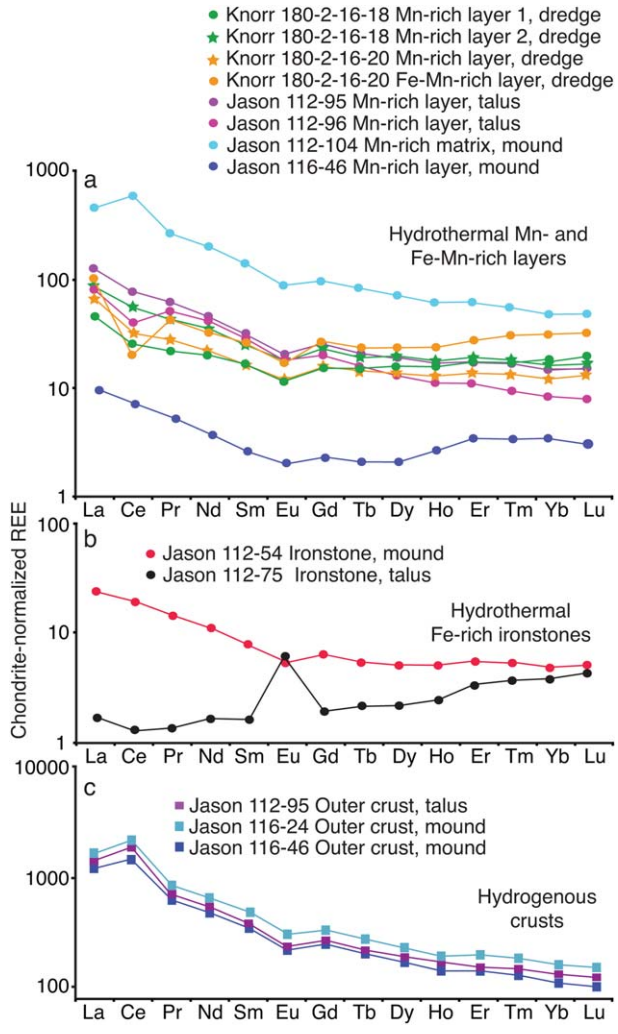

Figure 15. Chondrite-normalized REE patterns of samples analyzed for geochemistry. (a) Hydrothermal Mn oxides and Fe oxyhydroxides in layered sediments and mound samples. (b) Hydrothermal ironstones in layered sediments from mound and talus. (c) Hydrogenous surficial crusts.

and is similar to ironstones from Pacific seamounts described by *Hein et al*. [1994]. This similarity is further exemplified by its chondrite-normalized REE pattern (Figure 15b), which shows enrichment in the LREE with a small negative Eu anomaly [*Hein et al*., 1994]. In contrast, J112-75 exhibits depletion of the LREE and a strong positive Eu anomaly. This pattern is very similar to a silica-rich Fe oxide recovered from the TAG mound at 26°N on the MAR [*Mills and Elderfield*, 1995]. It is also similar to that of typical hydrothermal fluids such as the black and white smoker fluids at the TAG and Snakepit hydrothermal fields on the MAR [e.g., *Mills and Elderfield*, 1995; *Mitra et al*., 1994] although absolute abundances of REE are higher. This suggests that the mixed fluid from which the goethite precipitated in sample J112-75 contained a greater component of pure end-member hydrothermal fluid than that from which the goethite in sample J112-54 precipitated.

7.2. Mn-Rich Breccia Matrix

[55] Like the Mn-rich stratabound layers, the birnessite matrix from breccia sample J112-104 (Figures 7b and 11f) plots at the Mn apex (Fe/Mn ratio = 0.14) of the ternary diagram (Figure 14), indicating that it precipitated from hydrothermal fluid as it percolated through igneous rock debris and cemented it to form a breccia. This sample has higher Co (1760 ppm), Ni (4380 ppm), Pb (25 ppm), and Ce (358 ppm) contents, and also a higher Co/Zn ratio of 1.38, than the Mn-rich stratabound layers in other samples. In addition, it has a greater abundance of REE compared to the Mn-rich layers (total REE of 667 ppm compared

with 12–125 ppm) and a chondrite-normalized REE pattern that is enriched in LREE with a positive Ce anomaly (Figure 15a). This, together with the enrichment in trace elements, suggests that there may be a hydrogenous component in the matrix. This is likely to be either amorphous or poorly crystallized Mn oxides and Fe oxyhydroxides because the only mineral identified by XRD in the sample was birnessite. The high trace element contents could be due to coprecipitation with the hydrogenous Fe-Mn phases or to adsorption onto the surfaces of hydrogenous colloidal Fe oxyhydroxides.

[56] The hydrogenous component in this mixed-origin breccia matrix can be estimated by simple mixing using the Co concentrations of the hydrogenous and hydrothermal end-member components [*Hein et al*., 1996; *Manheim and Lane-Bostwick*, 1988]. Assuming that the three relatively pure stratabound Mn-rich layers (Co contents 100–323 ppm) represent the low-temperature hydrothermal end member and the three outer crusts (Co contents 4380–6640 ppm) represent the hydrogenous end-member, then the hydrogenous contribution to this breccia matrix is between 22% and 38%.

7.3. Hydrogenous Fe-Mn Crusts

[57] In contrast to the strong fractionation of iron and manganese observed in the hydrothermal Fe-Mn layers and ironstones, three hydrogenous Fe-Mn crusts (J112-95, Figure 11e; J116-24, Figure S1; J116-46, Figure 10) show little fractionation. They have Fe contents of 16.0–19.3 wt.% and Mn contents of 13.3–16.1 wt.%, resulting in Fe/Mn ratios of 1.0–1.4 that are consistent with hydrogenous accumulation from seawater. Their relatively high Co (4380–6640 ppm) and Ni concentrations (1230–4060 ppm), which are indicative of slow hydrogenous accumulation and oxidative scavenging from seawater, place them in the field for hydrogenous deposits in the Fe/Mn/Co + Ni + Cu ternary diagram (Figure 14). In addition, their high Pb (675–1000 ppm), Sr (1058–1247 ppm), and Ce (923–1310 ppm) contents and the high Co/Zn ratios (5.3–15.1) are typical of hydrogenous Fe-Mn crusts and nodules [*Hein et al*., 1997]. *Bonatti et al*. [1972] have used the U/Th ratio to distinguish between hydrogenous (lower U/Th ratios) and hydrothermal (higher U/Th ratios) Fe-Mn deposits because of incorporation of Th into Fe-Mn crusts during their extremely slow growth. Our Fe-Mn crust samples contain very high concentrations of Th (53–63 ppm), which results in low U/Th ratios of 0.16–0.18, and this further supports a hydrogenous origin of the crusts.

[58] Rare-earth elements are very abundant in the hydrogenous crusts, with totals ranging from 1705 to 2370 ppm. The chondrite-normalized REE patterns are all similar and show enrichment in LREEs with a positive Ce anomaly due to its concentration in Fe-Mn crusts by oxidation reactions (Figure 15c). Such patterns are typical for hydrogenous crusts that are inferred to accumulate at <10 mm m.y.$^{-1}$ [*Kuhn et al*., 1998].

[59] Using the empirical relation between Co content and growth rate derived by *Puteanus and Halbach* [1988], the three crusts analyzed give a range in growth rates of 3–6 mm m.y.$^{-1}$, consistent with their REE patterns. Based on observed crust thicknesses of 5–10 mm, these samples have been exposed to seawater for 1–3 m.y., in agreement with the $\sim$2.1–3.3 Ma age of the exposed detachment surface.

8. Discussion

8.1. Nature of Hydrothermal Venting at Mounds

[60] Fe-Mn hydrothermal precipitates sampled across the detachment surface of Kane Megamullion clearly demonstrate the presence of low-temperature hydrothermal venting, and occurrence of the precipitates in mounds indicates that mound formation is linked to the venting. The general restriction of mounds to the intact detachment surface and the near-absence of mounds in slump scars, as well as the fact that mounds contain large amounts of igneous rock and chalk debris, suggest that the mounds developed along the interface between the footwall and hanging wall of the detachment fault when it was active at the ridge axis.

[61] There is only limited evidence for high-temperature hydrothermal activity. The quartz-chlorite mineralogy of the breccia matrix in mound sample J116-24 (Figure S1) indicates high-temperature fluid flow, but the sample may have been displaced from another location, and it is not clear that formation of the mound was directly linked to that flow. If there was a direct link, the venting likely occurred in the hanging wall near the trace of the detachment in the rift valley. Other evidence for possible high-temperature fluids at Kane Megamullion comes from Adam Dome, where dredged fossil gastropods have been

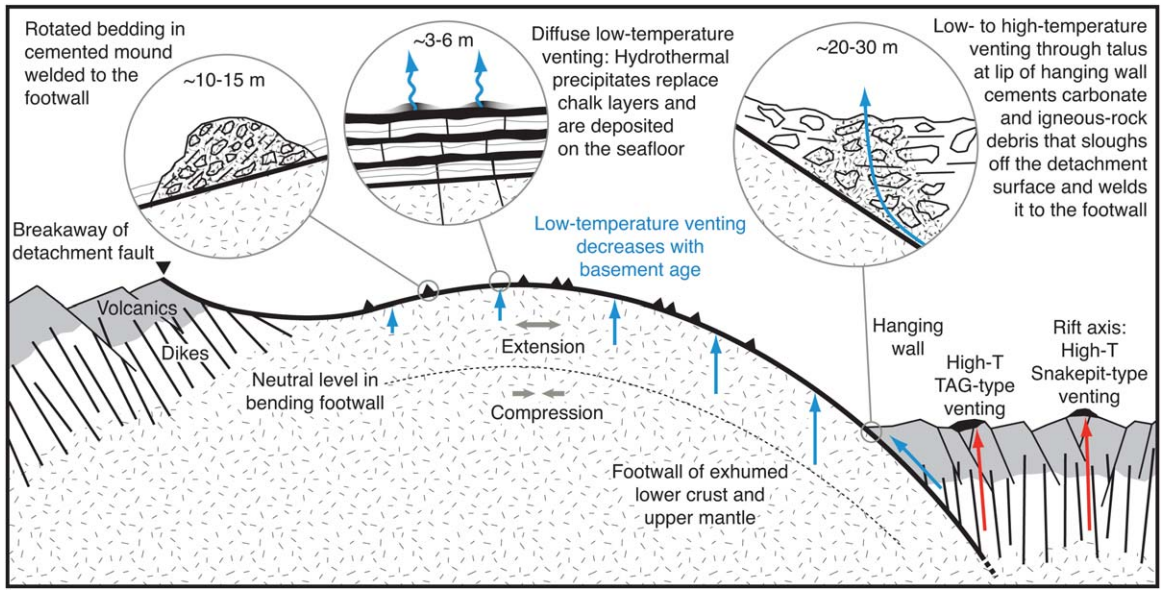

Figure 16. Schematic model for origin of mounds and layered hydrothermal sediments. Although high temperature, TAG- or Snakepit-type venting could be active within the rift valley (red arrows), fluids flowing up the detachment fault (blue arrow) appear to be mostly low-temperature near the footwall/hanging-wall contact. They exit the seafloor through the lip of the hanging wall, cement hanging-wall debris (patterned in inset), and weld it to the footwall. As the footwall is exhumed, surrounding unconsolidated debris sloughs off the detachment-fault surface, leaving isolated mounds of cemented debris (black triangles) that are transported off-axis and rotate with rollover of the footwall. Low-temperature hydrothermal fluids also exit from the bending footwall (blue arrows), which is compressed in its lower part and extended in its upper part. These fluids deposit Fe-Mn minerals on and within pelagic carbonates on the detachment surface. Approximate scales of insets are indicated.

identified as a new species of *Provannidae* (Figure 1) [*Kaim et al*., 2012]. These provannids are the first to be documented in the Atlantic Ocean, and where they are known in other ocean basins they are associated only with high-temperature hydrothermal vents.

[62] Although talc-rich serpentine rocks recovered across Kane Megamullion indicate high-temperature fluid-rock reactions along the detachment fault at depth [*Dick et al*., 2008], there is little information to constrain how high-temperature fluids circulated in the larger detachment system. In the following discussion, we restrict our interpretations to aspects of low-temperature fluid flow.

8.2. Model for Formation of Mounds

[63] We propose a model for hydrothermal venting and formation of mounds at Kane Megamullion as shown in Figure 16. In this model, mounds form where dominantly low-temperature hydrothermal springs well up through the lip of the detachment hanging wall at the side of the rift valley. Hydrothermal precipitates from the cooling fluids, perhaps accompanied by dissolution and reprecipitation of carbonates, cement hanging-wall debris and weld it to the footwall. The cemented debris persists as mounds on the footwall as it is exhumed while surrounding loose debris is shed down the exposed fault surface, which probably dips ~35° [*Tucholke et al*., 1998].

[64] Mounds should rotate with rollover of the footwall as they are transported off-axis (Figure 16), and this should be reflected in their depositional structure. Figure 8 shows an example of such rotation, with beds having an apparent dip of about 35° away from the spreading axis. The orientation is consistent with the expected direction and magnitude of rotation of the Kane detachment surface, which in the area of this mound is now nearly horizontal. In addition to igneous rock debris, the mound contains large amounts of chalk clasts that probably sloughed off the footwall.

[65] Variations in surface characteristics and compositions of mounds may be explained primarily by two factors: (1) the size of the zone in which hydrothermal fluids upwelled, together with lateral variations in flux; and (2) the depth within the hanging wall at which most mineral precipitation occurred. With respect to the first factor, the size

of the upwelling area would determine the amount of hanging-wall debris cemented and thus the size of the resultant mound. Some very large mounds appear to have subsidiary, smaller mounds on their surface. The smaller mounds probably formed where the shallowest flow was localized or where small springs persisted during the last stages of venting. Similarly, the cores of mounds (e.g., Figure 7b) and breccia boulders (Figures 6c and S1) may represent enhanced cementation where flow was most focused. In contrast, broadly distributed or diffuse flow might, at least in part, explain debris "fences," ridges, and other irregular accumulations of rock debris on the detachment surface.

[66] The depth within the hanging wall at which most hydrothermal precipitation occurred may account for the striking differences in surficial morphology and internal composition of mounds, which ranges from nearly pure igneous rock debris (Figures 5a and 5b) to nearly complete chalk cover (Figures 6a, 6b, 7c, 7d, and 7f). If hydrothermal precipitation was mostly in the subsurface of the hanging wall, there would be little involvement of seafloor pelagic carbonates. Thus, mounds of dominantly igneous rock would be exposed when the cemented debris was exhumed and the overlying, unconsolidated material sloughed away. Presumably, bottom currents would keep the mounds relatively free of calcareous sediment that accumulated on the surrounding detachment surface. An alternate explanation for the lack of sediment on igneous rock mounds is that they formed much later on the detachment surface, in places where fluids vented through the exposed footwall. However, this idea is untenable because there is no reasonable mechanism to aggregate scattered rocks on the fault surface into the loci of the vents.

[67] In contrast to the above, if there was significant hydrothermal precipitation at and near the seafloor, the resulting mounds would incorporate both pelagic carbonates and hanging-wall igneous rock and chalk debris. The closer the venting was to the active fault trace, the more likely it would be for a mound to incorporate large amounts of calcareous material sloughing off the detachment footwall.

[68] There are several indications that hydrothermal precipitation inside mounds extended beyond simple one-for-one volume replacement of sediment while cementing hanging-wall debris. First, some mound samples are nearly pure hydrothermal precipitates that show little evidence of pre-existing sediment (e.g., sample J112-104, Figure 11f). Second, the buckled structure of chalks in some mounds (e.g., Figures 7c, 7d, and 7f) suggests that internal precipitation may have forced volume expansion that distorted the bedding. Finally, similar volume expansion might even have driven extrusion of hydrothermal precipitates from mounds (e.g., Figures 10a and 10b); it is not at all clear that the lineations on these precipitates represent extrusion striae rather than bedding exposed in broken fragments, but they do bear a striking resemblance to striae on extruded lava pillows.

[69] Quasi-annular structures on some mounds covered by chalks (Figures 7c and 7d) may also be related to precipitation of hydrothermal sediments. Chalks in the perimeters of these features exhibit irregular, contorted bedding that suggests compression associated with volume expansion, and we infer that the annuli may locate centers of focused fluid flow. Presumably, highly cemented mound cores underlie these features.

[70] There is no reason that hydrothermal mounds like those reported here should be unique to Kane Megamullion, but there are only very limited high-resolution observations available to assess whether they are present on other megamullions. *Tucholke et al*. [2001] observed, but did not sample, very similar, conical rock mounds on the surface of Dante's Domes megamullion at 26°40′N on the MAR, and they suggested that the cones are volcanic constructs because of the pillow-like shapes of the rock debris. Considering our observations at Kane Megamullion, it seems more likely that those cones are hydrothermal mounds. Farther north at Atlantis Massif megamullion, *Blackman et al*. [2002] observed rock debris in "rare patches of exposed bedrock" on the detachment surface of Central Dome, from which metabasalts were sampled [*Blackman et al*., 2002, their Figure 7c]. These may be analogous to the rock mounds at Kane Megamullion and thus have a similar origin.

8.3. Hydrothermal Effects in Sediments on the Detachment Surface

[71] Sediments capping the detachment surface in some areas are nearly pure Fe-Mn precipitates or are chalks that are highly enriched in these precipitates. Some of these have relatively flat bedding and limited internal distortion (Figure S3), whereas others are contorted and buckled into ridges (Figures 6e, 6f, 9, and S2). Some Fe-Mn minerals in the flat-bedded sediments may have precipitated from hydrothermal fluids that

discharged from the hanging wall. However, it is clear that fluids also emanated from the exposed footwall and flowed through the capping carbonates, where they precipitated hydrothermal minerals and replaced chalks. It seems unlikely that the flat-bedded sediments were at any time part of the hanging wall because, unlike the mounds, they did not aggregate significant amounts of hanging-wall debris; also, they do not show structural disruption that would be expected had they been transferred from the hanging wall to the footwall.

[72] Colloform textures in some of the hydrothermal Mn oxides suggest that the hydrothermal precipitates accumulated either on a free surface (the seafloor) or in voids or water-rich zones within chalks. The former idea is supported by the layered nature of pure Fe-Mn precipitates (e.g., Figure 11d) and also by interbedding with chalks where the contacts appear to be depositional rather than due to replacement of chalk (e.g., Figure S3).

[73] On the other hand, there is clear penetrative deposition of hydrothermal minerals in microchannels and asicular growth in some samples (Figures 11a, 11b, 12c, 12d, and 12e), which indicates fluid flow through the chalks and replacement of carbonates by hydrothermal precipitates. In some cases, the replacement affected only micritic carbonate while leaving foraminiferal tests intact (Figures 12c and 12d), while in other places, all carbonate including the foraminifera was replaced (Figure 12b). Where layered hydrothermal Fe-Mn deposits are directly associated with microchannels, it is possible that the layers are at least partially a replacement of chalk (Figures 11a and 11b). The penetrative deposition of Fe-Mn minerals in the chalks provides strong evidence for fluid venting from the exposed footwall.

[74] We suggest that diffuse venting from the exposed footwall may also explain the buckled sedimentary ridges (Figures 6e, 6f, 9, and S2). The buckling implies compression within the chalks, which could be accomplished by internal precipitation of hydrothermal minerals. The detachment footwall was subjected to internal compression in its lower part and extension in its upper part as it was exhumed and rolled over (Figure 16), and this could have facilitated fluid expulsion into the overlying sediments. Presumably, the extent of diffuse venting would diminish with age of the footwall as it cooled and as mineral precipitation sealed fluid pathways. Even so, the very thin coating of hydrogenous Mn on some contorted deposits as well as suggestions of recent mobility (Figures 9 and S2) imply geologically recent hydrothermal circulation in ~2.7 Ma basement on the central part of the megamullion.

[75] An alternate explanation for buckling of sediments is downslope creep, with compression occurring where the sliding mass met resistance. Some buckled ridges are oriented along the local strike of seafloor topography, which would be consistent with this explanation, but other ridges are oriented at high angles or orthogonal to the strike. Furthermore, downslope creep does not explain polygonal patterns of buckling in some areas (e.g., Figures 6e and 6f). Thus, we favor venting through the footwall as an important, if not dominant, factor in formation of the buckled ridges.

9. Conclusions

[76] We have documented the occurrence of numerous, 1–10 m high, cemented mounds of igneous rock and chalk debris that are widely distributed on the detachment-fault surface that forms the seafloor at Kane Megamullion. Debris in the mounds ranges from primarily igneous rock fragments (dominantly basalt, but with lesser amounts of gabbro and serpentinite) to mixed igneous rock and chalk clasts. The mounds are commonly associated with significant deposits of low-temperature hydrothermal Mn oxides and Fe oxyhydroxides that are mineralogically and geochemically distinct from hydrogenous crusts that coat most samples.

[77] We propose a model in which the mounds are formed by hydrothermal venting through the lip of the detachment hanging wall in the rift valley. Fluids flowing up along the fault zone cement pockets of hanging-wall debris and weld them to the detachment surface. As the footwall and cemented debris are exhumed, loose surrounding talus sloughs off the footwall, leaving isolated mounds that are transported off-axis on the detachment surface. Large, linear to irregular ridges of igneous rock ± chalk debris on the detachment surface may be similarly related to cementation by hydrothermal fluids.

[78] In addition to hydrothermal effects at mounds, sediments capping the detachment surface show that hydrothermal Fe-Mn-rich minerals accumulated at numerous other places across the megamullion, either together with pelagic carbonates (now partially cemented as chalks) or as nearly pure hydrothermal precipitates. Some Fe-Mn-rich deposits may have precipitated from hanging-wall vent fluids in the rift valley. However,

hydrothermal fluids also emanated from the exposed detachment footwall off-axis, where they precipitated Fe-Mn minerals that partially replaced overlying chalks. Some localities exhibit buckled ridges of contorted chalk that is rich in hydrothermal Fe-Mn minerals, and we suggest that these formed by off-axis hydrothermal precipitation within the chalks that forced volume expansion. Some of these contorted deposits have only a very thin veneer of hydrogenous Fe-Mn compared to 5–10 mm hydrogenous crusts on rocks elsewhere on the detachment surface, and one fresh exposure indicates recent disturbance within the sediment. These observations suggest that geologically recent low-temperature hydrothermal circulation has occurred at least 40 km off-axis in ~2.7 Ma crust.

[79] Our results build on previous studies of hydrothermal activity associated with major normal faults in oceanic crust and suggest that detachments such as that at Kane Megamullion, as well as the associated hanging walls and footwalls, incorporate numerous pathways for fluid flow while they are active at the spreading axis. In addition, it appears that diffuse low-temperature venting may persist in detachment footwalls for several million years off-axis. Thus, large volumes of crust in detachment fault systems, not just the damage zones of the faults, are affected by hydrothermal activity. This must be considered in future studies of fluid-rock interactions in these systems, composition and distribution of hydrothermal deposits both on- and off-axis, and evolution of heat flow at slow-spreading ridges.

Acknowledgments

[80] We are indebted to Knorr Cruise 180-2 Chief Scientist Maurice Tivey, members of the shipboard scientific party, the Jason ROV team, and the ABE group for their excellent support during seagoing operations. NSF grant 0118445 supported data acquisition and processing for Knorr Cruise 180-2. The Deep Ocean Exploration Institute at Woods Hole Oceanographic Institution supported research and analytical costs for this study. We thank Margaret Sulanowska for performing the XRD analyses and sample photography. We also thank Jim Hein, Rachel Mills, and Associate Editor Gretchen Früh-Green for constructive comments that helped to improve the manuscript.

References

Auzende, J.-M., M. Cannat, P. Gente, J.-P. Henriet, T. Juteau, J. Karson, Y. Lagabrielle, C. Mével, and M. Tivey (1993), Affleurements des roches profondes de la croûte océanique et du manteau sur le mur sud de la fracture Kane (Atlantique central): Observations par submersible, *C. R. Acad. Sci. Paris*, *317*, 1641–1648.

Auzende, J.-M., M. Cannat, P. Gente, J.-P. Henriet, T. Juteau, J. Karson, Y. Lagabrielle, C. Mével, and M. Tivey (1994), Observation of sections of oceanic crust and mantle cropping out on the southern wall of Kane FZ (N. Atlantic), *Terra Nova*, *6*, 143–148, doi:10.1111/j.1365-3121.1994.tb00647.x.

Beltenev, V., et al. (2007), A new hydrothermal field at 13°30′N on the Mid-Atlantic Ridge, *InterRidge News*, *16*, 9–10 and 60.

Blackman, D. K., et al. (2002), Geology of the Atlantis Massif (Mid-Atlantic Ridge, 30°N): Implications for the evolution of an ultramafic oceanic core complex, *Mar. Geophys. Res.*, *23*, 443–469.

Bonatti, E., T. Kraemer, and H. Rydell (1972), Classification and genesis of submarine iron-manganese deposits, in *Ferromanganese Deposits on the Ocean Floor*, edited by D. R. Horn, pp. 149–166, Off. for the Int. Decade of Ocean Explor., Natl. Sci. Found., Washington, D. C.

Boschi, C., et al. (2006), Mass transfer and fluid flow during detachment faulting and development of an oceanic core complex, Atlantis Massif (MAR 30°N), *Geochem. Geophys. Geosyst.*, *7*, Q01004, doi:10.1029/2005GC001074.

Boström, K., and L. Widenfalk (1984), The origin of iron-rich muds at the Kameni Islands, Santorini, Greece, *Chem. Geol.*, *42*, 203–218.

Cann, J. R., D. K. Blackman, D. K. Smith, E. McAllister, B. Janssen, S. Mello, E. Avgerinos, A. R. Pascoe, and J. Escartín (1997), Corrugated slip surfaces formed at ridge-transform intersections on the Mid-Atlantic Ridge, *Nature*, *385*, 329–332.

Davydov, M. P., P. A. Aleksandrov, E. N. Perova, and T. A. Semkova (2007), Ferromanganese deposits in the Ashadze-1 hydrothermal field (Mid-Atlantic Ridge, 12° 48'S), *Dokl. Earth Sci.*, *415A*, 954–960.

De Carlo, E. H., G. M. McMurtry, and H.-W. Yeh (1983), Geochemistry of hydrothermal deposits from Loihi submarine volcano, Hawaii, *Earth Planet. Sci. Lett.*, *66*, 438–449.

deMartin, B. J., R. A. Sohn, J. P. Canales, and S. E. Humphris (2007), Kinematics and geometry of active detachment faulting beneath the Trans-Atlantic Geotraverse (TAG) hydrothermal field on the Mid-Atlantic Ridge, *Geology*, *35*, 711–714, doi:10.1130/G23718A.

Dick, H. J. B., G. Thompson, and W. B. Bryan (1981), Low angle faulting and steady-state emplacement of plutonic rocks at ridge-transform intersections, *Eos Trans. AGU*, *62*, 406.

Dick, H. J. B., M. A. Tivey, and B. E. Tucholke (2008), Plutonic foundation of a slow-spreading ridge segment: Oceanic core complex at Kane Megamullion, 23°30′N, 45°20′W, *Geochem. Geophys. Geosyst.*, *9*, Q05014, doi:10.1029/2007GC001645.

Escartín, J., G. Hirth, and B. Evans (2001), Strength of slightly serpentinized peridotites: Implications for the tectonics of oceanic lithosphere, *Geology*, *29*, 1023–1026.

Escartín, J., D. K. Smith, J. Cann, H. Schouten, C. H. Langmuir, and S. Escrig (2008), Central role of detachment faults in accretion of slow-spreading oceanic lithosphere, *Nature*, *455*, 790–794, doi:710.1038/nature07333.

Floyd, J. S., J. C. Mutter, A. M. Goodliffe, and B. Taylor (2001), Evidence for fault weakness and fluid flow within an active low-angle normal fault, *Nature*, *411*, 779–782.

Hein, J. R., M. S. Schulz, and L. M. Gein (1992), Central Pacific cobalt-rich ferromanganese crusts: Historical perspective and regional variability, in *Geology and Offshore Mineral Resources of the Central Pacific Basin*, edited by B. H. Keating and B. R. Bolton, pp. 261–283, Springer, New York.

Hein, J. R., H.-W. Yeh, S. H. Gunn, A. E. Gibbs, and C.-H. Wang (1994), Composition and origin of hydrothermal ironstones from central Pacific seamounts, *Geochim. Cosmochim. Acta*, *58*, 179–189.

Hein, J. R., A. E. Gibbs, D. A. Clague, and M. Torresan (1996), Hydrothermal mineralization along submarine rift zones, Hawaii, *Mar. Georesour. Geotechnol.*, *14*, 177–203.

Hein, J. R., A. Koschinsky, P. Halbach, F. T. Manheim, M. Bau, J.-K. Kang, and N. Lubick (1997), Iron and manganese oxide mineralization in the Pacific, in *Manganese Mineralization: Geochemistry and Mineralogy of Terrestrial and Marine Deposits*, edited by K. Nicholson, et al., Geol. Soc. Spec. Publ., *119*, 123–138.

Hein, J. R., A. Koschinsky, and B. R. McIntyre (2005), Mercury- and silver-rich ferromanganese oxides, southern California borderland: Deposit model and environmental implications, *Econ. Geol.*, *100*, 1151–1168.

Kaim, A., B. E. Tucholke, and A. Warén (2012), A new Late Pliocene large provannid gastropod associated with hydrothermal venting at Kane Megamullion, Mid-Atlantic Ridge, *J. Syst. Palaeontol.*, *10*, 423–433, doi:10.1080/14772019.2011.607193.

Karson, J. A. (1990), Seafloor spreading on the Mid-Atlantic Ridge: Implications for the structure of ophiolites and oceanic lithosphere produced in slow-spreading environments, in *Proceedings of the Symposium TROODOS 1987*, edited by J. Malpas, et al., pp. 547–555, Geol. Surv. Dept. Nicosia, Cyprus.

Kelley, D. S., et al. (2001), An off-axis hydrothermal vent field near the Mid-Atlantic Ridge at 30°N, *Nature*, *412*, 145–149.

Kuhn, T., M. Bau, N. Blum, and P. Halbach (1998), Origin of negative Ce anomalies in mixed hydrothermal-hydrogenetic crusts from the central Indian Ridge, *Earth Planet. Sci. Lett.*, *163*, 207–220.

Lalou, C., E. Brichet, T. L. Ku, and C. Jehanno (1977), Radiochemical, scanning electron microscope (SEM) and X-ray dispersive energy (EDAX) studies of a famous hydrothermal deposit, *Mar. Geol.*, *24*, 245–258.

MacLeod, C. J., R. C. Searle, B. J. Murton, J. F. Casey, C. Mallows, S. C. Unsworth, K. L. Achenbach, and M. Harris (2009), Life cycle of oceanic core complexes, *Earth Planet. Sci. Lett.*, *287*, 333–344, doi: 10.1016/j.epsl.2009.08.016.

Manheim, F. T., and C. M. Lane-Bostwick (1988), Cobalt in ferromanganese crusts as a monitor of hydrothermal discharge on the Pacific sea floor, *Nature*, *335*, 59–62.

Mills, R. A., and H. Elderfield (1995), Rare earth element geochemistry of hydrothermal deposits from the active TAG Mound, 26°N Mid-Atlantic Ridge, *Geochim. Cosmochim. Acta*, *59*, 3511–3524.

Mills, R. A., D. M. Wells, and S. Roberts (2001), Genesis of ferromanganese crusts from the TAG hydrothermal field, *Chem. Geol.*, *176*, 283–293.

Mitra, A., H. Elderfield, and M. J. Greaves (1994), Rare earth elements in submarine hydrothermal fluids and plumes from the Mid-Atlantic Ridge, *Mar. Chem.*, *46*, 217–236.

Petersen, S., K. Kuhn, T. Kuhn, N. Augustin, R. Hékinian, L. Franz, and C. Borowski (2009), The geological setting of the ultramafic-hosted Logatchev hydrothermal field (14°45'N, Mid-Atlantic Ridge) and its influence on massive sulfide formation, *Lithos*, *112*, 40–56, doi:10.1016/j.lithos.2009.02.008.

Puteanus, D., and P. Halbach (1988), Correlation of Co concentration and growth rate - A method for age determination of ferromanganese crusts, *Chem. Geol.*, *69*, 73–85.

Puteanus, D., D. P. Glasby, P. Stoffers, and H. Kunzendorf (1991), Hydrothermal iron-rich deposits from the Teahitia-Mehitia and Macdonald hot spot areas, southwest Pacific, *Mar. Geol.*, *98*, 389–409.

Rona, P. A., G. Klinkhammer, T. A. Nelsen, J. H. Trefry, and H. Elderfield (1986), Black smokers, massive sulfides and vent biota at the Mid-Atlantic Ridge, *Nature*, *321*, 33–37.

Schroeder, T., and B. E. John (2004), Strain localization on an oceanic detachment fault system, Atlantis Massif, 30°N, Mid-Atlantic Ridge, *Geochem. Geophy. Geosyst.*, *5*, Q11007, doi:10.1029/2004GC000728.

Smith, D. K., J. Escartín, H. Schouten, and J. R. Cann (2008), Fault rotation and core complex formation: Significant processes in seafloor formation at slow-spreading mid-ocean ridges (Mid-Atlantic Ridge, 13°–15°N), *Geochem. Geophys. Geosyst.*, *9*, Q03003, doi:10.1029/2007GC001699.

Thompson, G., M. J. Mottl, and P. A. Rona (1985), Morphology, mineralogy and chemistry of hydrothermal deposits from the TAG area, 26°N, Mid-Atlantic Ridge, *Chem. Geol.*, *49*, 243–257.

Toth, J. R. (1980), Deposition of submarine crusts rich in manganese and iron, *Geol. Soc. Am. Bull.*, *91*, 44–54.

Tucholke, B. E., and J. Lin (1994), A geological model for the structure of ridge segments in slow spreading ocean crust, *J. Geophys. Res.*, *99*, 11,937–11,958.

Tucholke, B. E., J. Lin, and M. C. Kleinrock (1996), Mullions, megamullions, and metamorphic core complexes on the Mid-Atlantic Ridge, *Eos Trans. AGU*, *77*(46), Fall Meet. Suppl., F724.

Tucholke, B. E., J. Lin, and M. C. Kleinrock (1998), Megamullions and mullion structure defining oceanic metamorphic complexes on the Mid-Atlantic Ridge, *J. Geophys. Res.*, *103*, 9857–9866.

Tucholke, B. E., K. Fujioka, T. Ishihara, G. Hirth, and M. Kinoshita (2001), Submersible study of an oceanic megamullion in the central North Atlantic, *J. Geophys. Res.*, *106*, 16145–16161.

Tucholke, B. E., M. D. Behn, W. R. Buck, and J. Lin (2008), Role of melt supply in oceanic detachment faulting and formation of megamullions, *Geology*, *36*, 455–458, doi:10.1130/G24639A.1.

Williams, C. M. (2007), Oceanic lithosphere magnetization: Marine magnetic investigations of crustal accretion and tectonic processes in mid-ocean ridge environments, PhD thesis, 285 pp., Mass. Inst. of Technol. and Woods Hole Oceanogr. Inst., Woods Hole, Mass.